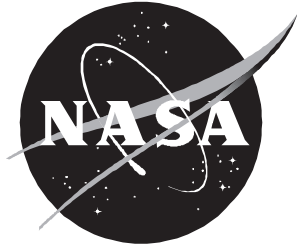


NASA/TP-2000-209865



An Improved Neutron Transport Algorithm for Space Radiation

*John H. Heinbockel and Martha S. Cloudsley
Old Dominion University, Norfolk, Virginia*

*John W. Wilson
Langley Research Center, Hampton, Virginia*

March 2000

The NASA STI Program Office . . . in Profile

Since its founding, NASA has been dedicated to the advancement of aeronautics and space science. The NASA Scientific and Technical Information (STI) Program Office plays a key part in helping NASA maintain this important role.

The NASA STI Program Office is operated by Langley Research Center, the lead center for NASA's scientific and technical information. The NASA STI Program Office provides access to the NASA STI Database, the largest collection of aeronautical and space science STI in the world. The Program Office is also NASA's institutional mechanism for disseminating the results of its research and development activities. These results are published by NASA in the NASA STI Report Series, which includes the following report types:

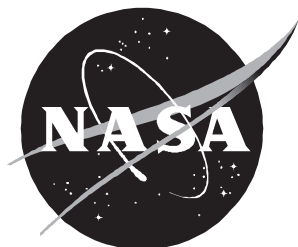
- **TECHNICAL PUBLICATION.** Reports of completed research or a major significant phase of research that present the results of NASA programs and include extensive data or theoretical analysis. Includes compilations of significant scientific and technical data and information deemed to be of continuing reference value. NASA counterpart of peer-reviewed formal professional papers, but having less stringent limitations on manuscript length and extent of graphic presentations.
- **TECHNICAL MEMORANDUM.** Scientific and technical findings that are preliminary or of specialized interest, e.g., quick release reports, working papers, and bibliographies that contain minimal annotation. Does not contain extensive analysis.
- **CONTRACTOR REPORT.** Scientific and technical findings by NASA-sponsored contractors and grantees.
- **CONFERENCE PUBLICATION.** Collected papers from scientific and technical conferences, symposia, seminars, or other meetings sponsored or co-sponsored by NASA.
- **SPECIAL PUBLICATION.** Scientific, technical, or historical information from NASA programs, projects, and missions, often concerned with subjects having substantial public interest.
- **TECHNICAL TRANSLATION.** English-language translations of foreign scientific and technical material pertinent to NASA's mission.

Specialized services that complement the STI Program Office's diverse offerings include creating custom thesauri, building customized databases, organizing and publishing research results . . . even providing videos.

For more information about the NASA STI Program Office, see the following:

- Access the NASA STI Program Home Page at <http://www.sti.nasa.gov>
- Email your question via the Internet to help@sti.nasa.gov
- Fax your question to the NASA STI Help Desk at (301) 621-0134
- Telephone the NASA STI Help Desk at (301) 621-0390
- Write to:
NASA STI Help Desk
NASA Center for AeroSpace Information
7121 Standard Drive
Hanover, MD 21076-1320

NASA/TP-2000-209865



An Improved Neutron Transport Algorithm for Space Radiation

*John H. Heinbockel and Martha S. Cloudsley
Old Dominion University, Norfolk, Virginia*

*John W. Wilson
Langley Research Center, Hampton, Virginia*

National Aeronautics and
Space Administration

Langley Research Center
Hampton, Virginia 23681-2199

March 2000

Available from:

NASA Center for AeroSpace Information (CASI)
7121 Standard Drive
Hanover, MD 21076-1320
(301) 621-0390

National Technical Information Service (NTIS)
5285 Port Royal Road
Springfield, VA 22161-2171
(703) 605-6000

Abstract

A low-energy neutron transport algorithm for use in space radiation protection is developed. The algorithm is based upon a multigroup analysis of the straight-ahead Boltzmann equation by using a mean value theorem for integrals. This analysis is accomplished by solving a realistic but simplified neutron transport test problem. The test problem is analyzed by using numerical and analytical procedures to obtain an accurate solution within specified error bounds. Results from the test problem are then used for determining mean values associated with rescattering terms that are associated with a multigroup solution of the straight-ahead Boltzmann equation. The algorithm is then coupled to the Langley HZETRN code through the evaporation source term. Evaluation of the neutron fluence generated by the solar particle event of February 23, 1956, for a water and an aluminum-water shield-target configuration is then compared with LAHET and MCNPX Monte Carlo code calculations for the same shield-target configuration. The algorithm developed showed a great improvement in results over the unmodified HZETRN solution. In addition, a two-directional solution of the evaporation source showed even further improvement of the fluence near the front of the water target where diffusion from the front surface is important.

Introduction

The purpose of this paper is to present an improved algorithm for the analysis of the transport of low-energy neutrons arising in space radiation protection studies. The design and operational processes in space radiation shielding and protection require highly efficient computational procedures to adequately characterize time-dependent environments, time-dependent geometric factors, and to address shield evaluation issues in a multidisciplinary integrated engineering design environment. One example is the recent study of the biological response in exposures to space solar particle events (SPE's) in which the changing quality of the radiation fields at specific tissue sites is followed over 50 hours of satellite data to evaluate time-dependent factors in biological response of the hematopoietic system (ref. 1). Similarly, the study of cellular repair dependent effects on the neoplastic cell transformation of a $C3H10T \frac{1}{2}$ population in low Earth orbit, where trapped radiations and galactic cosmic rays vary continuously in intensity and spectral content about the orbital path (ref. 2), requires computationally efficient codes to match time-dependent boundary conditions around the orbital path. But even in a steady environment which is homogeneous and isotropic, the radiation fields within a spacecraft have large spatial gradients and highly anisotropic factors so that the mapping of the radiation fields within the astronaut's tissues depends on the astronaut timeline of location and orientation within the spacecraft interior where large differences in exposure patterns that depend on the activity of the astronaut have been found (ref. 3). Obvious cases exist where rapid evaluation of exposure fields of specific tissues are required to describe the effects of variations in the time-dependent exterior environment or changing geometric arrangement. A recent study of the time-dependent response factors for 50 hours of exposure to the SPE of August 4, 1972, required 18 CPU hours on a VAX 4000/500 computer by using the nucleon-light ion section of the deterministic high charge and energy transport code HZETRN. The related calculation with a standard Monte Carlo code such as HETC or LAHET, which only handles neutrons, protons, pions, and alphas, would have required approximately 2 years of computer time to complete the study. The design environment also requires rapid evaluation of the radiation fields to adequately determine effects of multiparameter design changes on system performance (refs. 4 and 5). These effects are the

driving factors in the development and use of deterministic codes and in particular the HZETRN code system that handles all naturally occurring atomic ions and neutrons.

The basic philosophy for the development of the deterministic HZETRN code began with the study by Alsmiller et al. (ref. 6) with an early version of HETC, wherein they demonstrated that the straight-ahead approximation for broad beam exposures was adequate for evaluation of exposure quantities. Wilson and Khandelwal (ref. 7) examined the effects of beam divergence on the estimation of exposure in arbitrary convex geometries and demonstrated that the errors in the straight-ahead approximation are proportional to the square of the ratio of the beam divergence to the radius of curvature, which is small in typical space applications. From a shielding perspective, the straight-ahead approximation overestimates the transmitted flux, and the error is found to be small in space radiation exposure quantities. Our first implementation of a numerical procedure was performed by Wilson and Lamkin (ref. 8) as a numerical iterative procedure of the charged components perturbation series expansion of the Boltzmann transport equation and showed good agreement with Monte Carlo calculations for modest penetrations to where neutrons play an important role. The neutron component was added by Lamkin (ref. 9); this closed the gap between the deterministic code and the Monte Carlo code. The resulting code was fast compared with the Monte Carlo codes but still lacked efficiency in generating and handling large data arrays, which would be solved in the next generation of codes.

The transport of high-energy ions is well adapted to the straight-ahead approximation. In fact, a more common assumption that secondary ion fragments are produced with the same velocity as the primary initial ion (ref. 10) is inferior to the straight-ahead approximation contrary to intuition (ref. 11). The Boltzmann transport equation for the particle fields $\phi_j(x, E)$ is given in the straight-ahead and continuous slowing down approximations as

$$\left[\frac{\partial}{\partial x} - \frac{\partial}{\partial E} S_j(E) + \sigma_j(E) \right] \phi_j(x, E) = \int_E^\infty \sigma_{jk}(E, E') \phi_k(x, E') dE' \quad (1)$$

where x is the depth of penetration, E is the particle kinetic energy, $S_j(E)$ is the particle stopping power, $\sigma_j(E)$ is the macroscopic interaction cross section, and $\sigma_{jk}(E, E')$ is the macroscopic cross section for particle k of energy E' produced as a result of the interaction with a particle j of energy E . At Langley Research Center for all the code development, it has been customary to invert the differential operator and implement it exactly as a marching procedure (ref. 12), and the remaining issue has been in approximating the integral term on the right-hand side of equation (1). The implementation for the heavy fragments was facilitated by the assumption that the fragment velocity is the same as the primary ion which is inadequate for the description of the coupled nucleonic and light ion components. A compatible nucleonic transport procedure was developed by Wilson et al. (ref. 13) and showed good agreement with exposure quantities evaluated by Monte Carlo transport procedures (ref. 14). The transport of the nucleonic component was developed by assuming that the midpoint energy within the step was the appropriate energy to evaluate the integral term. Thus, the residual range of the proton will reduce by $h/2$ before the interaction and the secondary proton residual range will reduce by $h/2$ before arriving at the next marching step. Neutrons show no loss in residual range as their stopping power is zero. This choice was shown to minimize the second-order corrections to the marching procedure (ref. 15). Although reasonable agreement on exposure quantities from Monte Carlo calculations was obtained, the resultant neutron flux at the lowest energies was substantially below the Monte Carlo result in the range of 0.01 to several MeV and required improvement (ref. 16). Analysis concluded that the problem was in the rescattering terms in which the number of elastic scattered neutrons was underestimated numerically, which must be addressed as suggested by Shinn et al. (ref. 16).

The issue of evaluation of the integral term of the Boltzmann equation for the elastic scattering is the next issue to be resolved in the development of the HZETRN deterministic code. Once the elastic scattering events are adequately represented and the associated improvements in the neutron flux are made, one still needs to address the issue of the adequacy of the nuclear database for nucleonic transport in the HZETRN code system (ref. 13).

Formulation of Transport Equations

Define the differential operator B as

$$\begin{aligned} B[\phi] &= \left[\frac{\partial}{\partial x} - \frac{\partial}{\partial E} S_j(E) + \sigma_j(E) \right] \phi(x, E) \\ &= \frac{\partial \phi(x, E)}{\partial x} - \frac{\partial}{\partial E} [S_j(E) \phi(x, E)] + \sigma_j(E) \phi(x, E) \end{aligned} \quad (2)$$

and consider the following one-dimensional Boltzmann equation from reference 17

$$B[\phi_j] = \sum_k \int_0^\infty \sigma_{jk}(E, E') \phi_k(x, E') dE' \quad (3)$$

where ϕ_j is the differential flux spectrum for the type j particles, $S_j(E)$ is the stopping power of the type j particles, and $\sigma_j(E)$ is the total macroscopic cross section. The term $\sigma_{jk}(E, E')$, a macroscopic differential energy cross section for redistribution of particle type and energy, is written as

$$\sigma_{jk}(E, E') = \sum_\beta \rho_\beta \sigma_\beta(E') f_{jk,\beta}(E, E')$$

where $f_{jk,\beta}(E, E')$ is the spectral redistribution, σ_β is a microscopic cross section, and ρ_β is the number density of β type atoms per unit mass. The spectral terms are expressed as

$$f_{jk,\beta} = f_{jk,\beta}^{\text{el}} + f_{jk,\beta}^e + f_{jk,\beta}^d$$

where $f_{jk,\beta}^{\text{el}}$ represents the elastic redistribution in energy, $f_{jk,\beta}^e$ represents evaporation terms, and $f_{jk,\beta}^d$ represents direct knockout terms. The elastic term is generally limited to a small energy range near that of the primary particle. The evaporation process dominates over the low energies ($E < 25$ MeV) and the direct cascading effect dominates over the high energy range ($E > 25$ MeV) as illustrated in figure 1.

Equation (3) is then written for $j = n$ as

$$B[\phi_n] = \sum_k \int_E^\infty \sum_\beta \rho_\beta \sigma_\beta(E') (f_{nk,\beta}^{\text{el}} + f_{nk,\beta}^e + f_{nk,\beta}^d) \phi_k(x, E') dE' \quad (4)$$

which is expanded to the form

$$\begin{aligned} B[\phi_n] &= \int_E^\infty \sum_\beta \rho_\beta \sigma_\beta(E') (f_{nn,\beta}^{\text{el}} + f_{nn,\beta}^e + f_{nn,\beta}^d) \phi_n(x, E') dE' \\ &\quad + \sum_{k \neq n} \int_E^\infty \sum_\beta \rho_\beta \sigma_\beta(E') (f_{nk,\beta}^{\text{el}} + f_{nk,\beta}^e + f_{nk,\beta}^d) \phi_k(x, E') dE' \end{aligned} \quad (5)$$

Define the integral operators I as

$$\begin{aligned} I_{\text{el}}^{(k)}[\phi] &= \int_E^\infty \sum_\beta \rho_\beta \sigma_\beta(E') f_{nk,\beta}^{\text{el}} \phi(x, E') dE' \\ I_e^{(k)}[\phi] &= \int_E^\infty \sum_\beta \rho_\beta \sigma_\beta(E') f_{nk,\beta}^e \phi(x, E') dE' \\ I_d^{(k)}[\phi] &= \int_E^\infty \sum_\beta \rho_\beta \sigma_\beta(E') f_{nk,\beta}^d \phi(x, E') dE' \end{aligned}$$

where $k = n$ denotes coupling to neutron collisions and $k = p$ denotes the neutron source from proton collisions. When considering only neutrons and protons, equation (5) can be written in the linear operator form as

$$B[\phi_n] = I_{\text{el}}^{(n)}[\phi_n] + I_e^{(n)}[\phi_n] + I_d^{(n)}[\phi_n] + I_{\text{el}}^{(p)}[\phi_p] + I_e^{(p)}[\phi_p] + I_d^{(p)}[\phi_p] \quad (6)$$

Note that $I_{\text{el}}^{(p)}[\phi_p]$ does not contribute to the neutron field; therefore, equation (6), with ϕ_n replaced by ϕ , is written as

$$B[\phi] = I_{\text{el}}^{(n)}[\phi] + I_e^{(n)}[\phi] + I_d^{(n)}[\phi] + I_e^{(p)}[\phi_p] + I_d^{(p)}[\phi_p] \quad (7)$$

Assume a solution to equation (7) of the form $\phi = \phi_e + \phi_d$, where ϕ_e is the solution for evaporation sources and contributes over the low-energy range and ϕ_d is the solution for the direct knockout sources and contributes mainly over the high-energy range as suggested by figure 1. Substitute this assumed solution into equation (7) and find

$$\begin{aligned} B[\phi] = B[\phi_e] + B[\phi_d] &= I_{\text{el}}^{(n)}[\phi_e] + I_{\text{el}}^{(n)}[\phi_d] + I_e^{(n)}[\phi_e] + I_e^{(n)}[\phi_d] \\ &\quad + I_d^{(n)}[\phi_e] + I_d^{(n)}[\phi_d] + I_e^{(p)}[\phi_p] + I_d^{(p)}[\phi_p] \end{aligned} \quad (8)$$

The terms $I_e^{(n)}[\phi_e]$ and $I_d^{(n)}[\phi_e]$ are near zero and are ignored because evaporation neutrons at low energies do not produce additional evaporation neutrons, and the direct cascade effects have very small cross sections over the low-energy range of ϕ_e and hence does not contribute any production over the low- or high-energy range. Further assume that ϕ_d is calculated by the HZETRN program so that ϕ_d is a solution of the equation

$$B[\phi_d] = I_{\text{el}}^{(n)}[\phi_d] + I_d^{(n)}[\phi_d] + I_d^{(p)}[\phi_p] \quad (9)$$

This assumption simplifies equation (8) to the form

$$B[\phi_e] = I_{\text{el}}^{(n)}[\phi_e] + I_e^{(n)}[\phi_d] + I_e^{(p)}[\phi_p] \quad (10)$$

Define the elastic scattering terms

$$\sigma_{s,\beta} = \rho_\beta \sigma_\beta(E') f_{jk,\beta}^{\text{el}}(E, E')$$

with units of $\text{cm}^2/\text{g-MeV}$, and note that for neutrons the stopping power $S_j(E)$ is zero and equation (10) reduces to the integro-differential transport equation with source term

$$\left[\frac{\partial}{\partial x} + \sigma(E) \right] \phi_e(x, E) = \sum_\beta \int_E^\infty \sigma_{s,\beta}(E, E') \phi_e(x, E') dE' + g(E, x) \quad (11)$$

Equation (11) represents the steady-state low-energy neutron fluence $\phi_e(x, E)$ at depth x and energy E . The various terms in equation (11) are energy E with units of MeV, depth in medium is x with units of g/cm², $\phi_e(x, E)$ (in particles/cm²-MeV) is the evaporation neutron fluence, and $g(E, x) = I_e^{(n)}[\phi_d] + I_e^{(p)}[\phi_p]$ (in particles/g-MeV) is a volume source term to be evaluated by the HZETRN algorithm. Equation (11) is further reduced by considering the neutron energies before and after a collision. The neutron energy E_n after an elastic collision with a nucleus of mass number $A_{T\beta}$, initially at rest, is, from reference 18,

$$E_n = E \left[\frac{A_{T\beta}^2 + 2A_{T\beta} \cos \theta + 1}{(A_{T\beta} + 1)^2} \right] \quad (12)$$

where E is the neutron energy before the collision, A_{T_i} is the atomic weight of the i th type of atom being bombarded, and θ is the angle of scatter. Define the ratio

$$\alpha_\beta = \left(\frac{A_{T\beta} - 1}{A_{T\beta} + 1} \right)^2 \quad (13)$$

as a constant less than 1 and note that when $\theta = 0$, $E_n = E$, and when $\theta = \pi$, $E_n = E\alpha_\beta$. Therefore, change the limits of integration in equation (11) to $(E, E/\alpha_\beta)$ which represent the kinetically allowed energies for the scattered neutron to result in an energy E . Equation (11) then is written as

$$\left[\frac{\partial}{\partial x} + \sigma(E) \right] \phi_e(x, E) = \sum_{\beta} \int_E^{E/\alpha_\beta} \sigma_{s,\beta}(E, E') \phi_e(x, E') dE' + g(E, x) \quad (14)$$

The quantity σ in cm²/g is a macroscopic cross section given by

$$\sigma = \sum_{\beta} \rho_{\beta} \sigma_{\beta} \quad (15)$$

where ρ_{β} is the number of atoms per gram and σ_{β} is a microscopic cross section in cm²/atom. Reference 19 provides approximate Maxwellian averages of cross-section values in barns which are used herein for studies of solution techniques. These values are listed in table 1 along with other parameters of interest for selected elements. Other units for equation (11) are obtained from the previous units by using the scale factor representing the density of the material in units of g/cm³.

Table 1. Parameter Values for Selected Elements

Element	$A_{T\beta}$	Elastic cross section, barns ^a	Density, g/cm ³	α_β
Lithium, Li	7	1.050	0.534	0.563
Carbon, C	12	4.739	0.352	0.716
Aluminum, Al	27	1.348	2.7	0.862
Calcium, Ca	40	2.99	1.54	0.905
Iron, Fe	56	11.40	7.85	0.931
Lead, Pb	207	11.194	11.342	0.981

^aMaxwellian averages (ref. 19).

Mean Value Theorem

Throughout the remaining discussions, the following mean value theorem is used for integrals.

Mean Value Theorem: For $\phi(x, E)$ and $f(E)$ continuous over an interval $a \leq E \leq b$ such that (1) $\phi(x, E)$ does not change sign over the interval (a, b) , (2) $\phi(x, E)$ is integrable over the interval (a, b) , and (3) $f(E)$ is bounded over the interval (a, b) , there exists at least one point ϵ such that

$$\int_a^b f(E) \phi(x, E) dE = f(\epsilon) \int_a^b \phi(x, E) dE \quad (a \leq \epsilon \leq b)$$

In particle transport, this mean value approach is not commonly used. In reactor neutron calculations, an assumed spectral dependence for $\phi(x, E)$ is used to approximate the integral over energy groups. The present use of the mean value theorem is free of these assumptions; thus, more flexibility is allowed in the HZETRN code, and the result is a fast and efficient algorithm for low neutron analysis.

Multigroup Method

Consider the case where there is only one value of β which represents neutron penetration into a single element material and let ϕ_ϵ be denoted by ϕ . Equation (14) is integrated from E_i to E_{i+1} with respect to the energy E to obtain

$$\int_{E_i}^{E_{i+1}} \frac{\partial \phi(x, E)}{\partial x} dE + \int_{E_i}^{E_{i+1}} \sigma(E) \phi(x, E) dE = I_i + \xi_i \quad (16)$$

where

$$I_i = \int_{E_i}^{E_{i+1}} \int_E^{E/\alpha_\beta} \sigma_{s,\beta}(E, E') \phi(x, E') dE' dE \quad (17)$$

and

$$\xi_i = \int_{E_i}^{E_{i+1}} g(E, x) dE \quad (18)$$

As a test case for developing solution techniques, we use the approximate source and scattering terms taken from subroutine FBERT of the HZETRN code (ref. 5), $g = g(E, x) = KEe^{-E/T}$

with K and T constants, and the elastic scattering term from subroutine ELSPEC of the HZETRN code (ref. 5),

$$\sigma_{s,\beta}(E, E') = \frac{\sigma(E') \tau e^{-\tau(E'-E)}}{1 - e^{-(1-\alpha)\tau E'}}$$

with τ constant, so that equation (18) is easily integrated to obtain

$$\xi_i = KT \left(E_i e^{-E_i/T} - E_{i+1} e^{-E_{i+1}/T} \right) + KT^2 \left(e^{-E_i/T} - e^{-E_{i+1}/T} \right) \quad (19)$$

The quantity

$$\Phi_i(x) = \int_{E_i}^{E_{i+1}} \phi(x, E) dE \quad (20)$$

is associated with the i th energy group, so that $\frac{1}{E_{i+1}-E_i} \Phi_i(x)$ represents an average fluence for each energy group. Then equation (16) can be written in terms of $\Phi_i(x)$ as follows. In the first term of equation (16), interchange the order of integration and differentiation to obtain

$$\int_{E_i}^{E_{i+1}} \frac{\partial \phi(x, E)}{\partial x} dE = \frac{d\Phi_i(x)}{dx} \quad (21)$$

With the previously stated mean value theorem for integrals, the second term in equation (16) can be expressed as

$$\int_{E_i}^{E_{i+1}} \sigma \phi(x, E) dE = \bar{\sigma} \Phi_i(x) \quad (22)$$

where $\bar{\sigma} = \sigma[E_i + \theta(E_{i+1} - E_i)]$, for some value of θ between 0 and 1.

For the term I_i in equation (17), the order of integration is interchanged. Various partitioning schemes are illustrated in figure 2. The integration of equation (17) depends upon the energy partition selected. For example, figure 2(b) illustrates an energy partition where $E_{i+1} < E_i/\alpha$, and in this case, equation (17) can be written as

$$I_i = \int_{E'=E_i}^{E_{i+1}} \int_{E=E_i}^{E'} H dE dE' + \int_{E'=E_{i+1}}^{E_i/\alpha} \int_{E=E_i}^{E_{i+1}} H dE dE' + \int_{E'=E_i/\alpha}^{E_{i+1}/\alpha} \int_{E=\alpha E'}^{E_{i+1}} H dE dE' \quad (23)$$

where $H = \sigma_s(E, E') \phi(x, E')$. Figure 2(c) depicts the case where $E_{i+1} = E_i/\alpha$ exactly for all i . In this special case, equation (17) reduces to

$$I_i = \int_{E'=E_i}^{E_{i+1}} \int_{E=E_i}^{E'} H dE dE' + \int_{E'=E_{i+1}}^{E_{i+1}/\alpha} \int_{E=\alpha E'}^{E_{i+1}} H dE dE' \quad (24)$$

The selection of an energy partition can lead to two or more distinct groups associated with each interchange in the order of integration (for example, see fig. 3). The integrand H can be integrated with respect to E and the results expressed in terms of the quantities

$$F(b, a) = \int_a^b \tau e^{\tau E} dE = e^{\tau b} - e^{\tau a}$$

and

$$G(E') = \frac{\sigma(E') e^{-\tau E'}}{1 - e^{-(1-\alpha)\tau E'}}$$

and equation (24) can be written in the form

$$I_i = \int_{E'=E_i}^{E_{i+1}} G(E') F(E', E_i) \phi(x, E') dE' + \int_{E'=E_{i+1}}^{E_{i+1}/\alpha} G(E') F(E_{i+1}, \alpha E') \phi(x, E') dE' \quad (25)$$

To illustrate the basic idea behind the multigroup method, use the same mean value theorem for integrals and write equation (25) in the form

$$I_i = G(E_i^*) F(E_i^*, E_i) \Phi_i + G(E_{i+1}^*) F(E_{i+1}, \alpha E_{i+1}^*) \Phi_{i+1}$$

where $E_i < E_i^* < E_i/\alpha$ and $E_{i+1} < E_{i+1}^* < E_{i+1}/\alpha$. The special partitioning of the energy as illustrated in figure 2(c) enables us to obtain from equation (16) a system of ordinary differential equations as follows:

$$\frac{d}{dx} \begin{bmatrix} \Phi_0 \\ \Phi_1 \\ \vdots \\ \Phi_{N-2} \\ \Phi_{N-1} \end{bmatrix} = \begin{bmatrix} a_{11} & a_{12} & & -0- \\ & a_{22} & a_{23} & \\ & & \ddots & \ddots \\ -0- & & a_{N-1,N-1} & a_{N-1,N} \\ & & & a_{NN} \end{bmatrix} \begin{bmatrix} \Phi_0 \\ \Phi_1 \\ \vdots \\ \Phi_{N-2} \\ \Phi_{N-1} \end{bmatrix} + \begin{bmatrix} \xi_0 \\ \xi_1 \\ \vdots \\ \xi_{N-2} \\ \xi_{N-1} \end{bmatrix} \quad (26)$$

where $a_{i,i} = G(E_i^*) F(E_i^*, E_i) - \bar{\sigma}$ and $a_{i,i+1} = G(E_{i+1}^*) F(E_{i+1}, \alpha E_{i+1}^*)$. Further assume that for large values of N , $\Phi_i = 0$ for all $i \geq N$. This assumption gives rise to the following system of ordinary differential equations:

$$\frac{d\bar{y}}{dx} = A\bar{y} + \bar{b}$$

subject to the initial conditions $\bar{y}(0) = \bar{0}$. Here \bar{y} is the column vector of Φ_i values, $\text{col}(\Phi_0, \Phi_1, \dots, \Phi_{N-1})$, the matrix A is an N by N upper triangular matrix, and \bar{b} is the column vector $\text{col}(\xi_0, \xi_1, \dots, \xi_{N-1})$. In a similar manner, the integrals in equation (23) can be evaluated for other kinds of energy partitioning and a system of equations having the form of equation (26) obtained. However, for these other energy partitions, the structure of the N by N square matrix A will change. It remains upper triangular but with more off-diagonal elements which depend upon the type of energy partition. (See, for example, fig. 3.) For our purposes the system of equations (eq. (26)) is used to discuss some of the problems associated with the multigroup method.

Of prime concern is how an energy grid is to be constructed and how this energy grid controls the size of the matrix in equation (26). Consider the construction of the energy partition

$$\left\{ E_0, \frac{E_0}{\alpha}, \frac{E_0}{\alpha^2}, \dots, \frac{E_0}{\alpha^N} \right\}$$

where $E_0 = 0.1$ MeV, for the selected elements of lithium, aluminum, and lead. Table 2 illustrates integer values of N necessary to achieve energies greater than 30 MeV. These values of N represent the size of the matrix associated with the number of energy groups. The value $E_0 = 0.1$ MeV, in terms of human exposure, represents a lower bound where lower energies are not important. The value of 30 MeV represents an upper limit for the evaporation particles.

Table 2. Energy Partition Size N

Element	α	N	$0.1/\alpha^N$
Lithium	0.563	10	31.53
Aluminum	0.862	39	32.75
Lead	0.981	298	30.38

Observe that for energy partitions where $E_{i+1} < E_i/\alpha$ the values of N are larger, and if $E_{i+1} > E_i/\alpha$ the values of N are smaller. The cases where $E_{i+1} > E_i/\alpha$ give rise to problems associated with the integration over the areas A_1 and A_2 of figure 2(d) when the order of integration is interchanged. In this figure, the area A_1 is associated with the integral defining Φ_i , and the area A_2 is a remaining area associated with an integral that is some fraction of the integral defining Φ_{i+1} which is outside the range of integration. Therefore, some approximation must be made to define this fractional part. This type of partitioning produces errors, due to any approximations, but it has the advantage of greatly reducing the size of the N by N matrix A at the cost of introducing errors into the system of equations. A more detailed analysis of the energy partition can be found in reference 20.

The case of neutron penetration into a composite material gives rise to the case where $\beta > 1$ in equation (11). In this special case, equation (17) becomes

$$I_i = \sum_j \int_{E_i}^{E_{i+1}} \int_E^{E/\alpha_j} \sigma_{sj}(E, E') \phi(x, E') dE' dE$$

Select $\alpha = \max(\alpha_1, \alpha_2, \dots, \alpha_j)$ and construct the energy partition where $E_{i+1} = E_i/\alpha$. Then obtain a system of differential equations having the upper triangular form:

$$\frac{d}{dx} \begin{bmatrix} \Phi_0 \\ \Phi_1 \\ \vdots \\ \vdots \\ \Phi_{N-1} \end{bmatrix} = \begin{bmatrix} a_{11} & a_{12} & a_{13} & \cdots & a_{1N} \\ & a_{22} & a_{23} & \cdots & a_{2N} \\ & & a_{33} & \cdots & \vdots \\ -0- & & & \ddots & \vdots \\ & & & & a_{NN} \end{bmatrix} \begin{bmatrix} \Phi_0 \\ \Phi_1 \\ \vdots \\ \vdots \\ \Phi_{N-1} \end{bmatrix} + \begin{bmatrix} \xi_0 \\ \xi_1 \\ \vdots \\ \vdots \\ \xi_{N-1} \end{bmatrix} \quad (27)$$

Observe that for some arbitrary energy grouping we have, for the element hydrogen, a case where the value of α_j is zero. In this situation we must integrate over many energy groups as illustrated in figure 3. Some type of approximations must be made when the order of integration is interchanged, depending upon the selected energy partitioning. Also the problem of selecting the mean values associated with each of these integrations exists.

Mean Value Determination

Consider the case of neutron fluence in a single shield material with the energy partitioning as illustrated in figure 2(c). This case is where successive energy values are given by $E_{i+1} = E_i/\alpha$ for all values of the index i as it ranges from 0 to N . Select a finite value for N large enough that the assumption $\Phi_N = 0$ holds true. The system of equations in equation (26) is then a closed system and we can solve for the last term Φ_N and then march backwards to solve $\Phi_{N-1}, \Phi_{N-2}, \dots$

The nonzero elements $a_{i,j}$ for matrix A in equation (26) consists of the diagonal elements and the first diagonal above the main diagonal. This gives the values

$$\begin{aligned} a_{ii} &= G(E_i^*) F(E_i^*, E_i) - \bar{\sigma} \\ a_{i,i+1} &= G(E_{i+1}^*) F(E_{i+1}, \alpha E_{i+1}^*) \end{aligned}$$

for $i = 1, \dots, N$, where E_i^* and E_{i+1}^* are selected mean values associated with the lower and upper triangles illustrated in figure 2(c). These mean values vary with energy and were selected so that the multigroup solution agrees with the numerical solution of the test problem. The values determined empirically were

$$\begin{aligned} E_i^* &= E_i + \theta_1 (E_{i+1} - E_i) \\ E_{i+1}^* &= E_{i+1} + \theta_2 (E_{i+2} - E_{i+1}) \end{aligned}$$

where

$$\theta_1 = \begin{cases} \gamma_1 + m_{11}(E - E_{11}) - \delta_1 & (E > E_{11}) \\ \gamma_1 + m_{12}(E - E_{11}) - \delta_1 & (E_{22} < E < E_{11}) \\ \gamma_3 + m_{13}(E - E_{22}) - \delta_1 & (E < E_{22}) \end{cases}$$

and

$$\theta_2 = \begin{cases} \gamma_2 + m_{21}(E - E_{11}) & (E > E_{11}) \\ \gamma_2 + m_{22}(E - E_{11}) & (E_{22} < E < E_{11}) \\ \gamma_4 + m_{23}(E - E_{22}) & (E < E_{22}) \end{cases}$$

where

$$\begin{aligned} \gamma_1 &= 0.93 & m_{11} &= 0.0030485 & m_{21} &= 0.004355 \\ \gamma_2 &= 0.90 & m_{12} &= 0.2490258 & m_{22} &= 0.249026 \\ \gamma_3 &= 0.30 & m_{13} &= -0.3937186 & m_{23} &= -0.255920 \\ \gamma_4 &= 0.27 & E_{11} &= 3.037829 & E_{22} &= 0.5079704 \end{aligned}$$

and δ_1 is 0.0 for lead, 0.02 for aluminum, and 0.075 for lithium. These values of θ for the mean value theorems were determined by trial and error so that the multigroup curves would have the correct shape and agree with the numerical solution. These selections for the mean values are not unique.

Solution Method in Shield Materials

Consider the energy partition $E_{i+1} = E_i/\alpha$ and the resulting system of differential equations (eq. (26)). The solution of this system of equations is obtained by first solving the last equation of the system. This equation has the form

$$\frac{d\Phi_{N-1}}{dx} = a_{NN}\Phi_{N-1} + \xi_{N-1}(x) \quad (\Phi_{N-1}(0) = 0)$$

and has the solution

$$\Phi_{N-1}(x) = e^{a_{NN}x} \left[\Phi_{N-1}(0) + \int_0^x \xi_{N-1}(s) e^{-a_{NN}s} ds \right]$$

which implies

$$\Phi_{N-1}(x_0 + \Delta x) = e^{a_{NN}\Delta x} \Phi_{N-1}(x_0) + e^{a_{NN}(x_0 + \Delta x)} \int_{x_0}^{x_0 + \Delta x} \xi_{N-1}(s) e^{-a_{NN}s} ds$$

Now consider each of the remaining equations above the last equation in equation (26). A typical equation from this stack has the form

$$\frac{d\Phi_{i-1}}{dx} = a_{ii}\Phi_{i-1} + f_i(x) \quad (\Phi_{i-1}(0) = 0) \quad (28)$$

where $f_i(x) = \xi_i(x) + a_{i,i+1}\Phi_i(x)$ is known, since $\Phi_i(x)$ is calculated before $\Phi_{i-1}(x)$. This typical equation has the solution

$$\Phi_{i-1}(x) = e^{a_{ii}x} \left[\Phi_{i-1}(0) + \int_0^x f_i(s) e^{-a_{ii}s} ds \right]$$

which implies

$$\Phi_{i-1}(x_0 + \Delta x) = e^{a_{ii}\Delta x} \Phi_{i-1}(x_0) + e^{a_{ii}(x_0 + \Delta x)} \int_{x_0}^{x_0 + \Delta x} f_i(s) e^{-a_{ii}s} ds$$

Observe that for the system of equations in equation (27), the solution technique is essentially the same with the exception that the right-hand side of equation (28) is replaced by a summation

of the previously calculated terms, so that $f_i(x) = \xi_i(x) + \sum_{j=i+1}^N a_{i,j} \Phi_{j-1}(x)$.

Numerical Solution

The solutions obtained from the system of equations (eq. (26) or (27)) depend upon the selection of mean values associated with each energy interval. The selection of these mean values is determined by examining the numerical solution in certain special cases. We obtain a numerical solution of equation (11) in the special case given by

$$g = g(E, x) = KEe^{-E/T}$$

where K (particles/cm³-MeV) and T (MeV) are constants. We construct the solution over the spatial domain $x \geq 0$ and energy range $0.1 \leq E \leq 80$ MeV. This domain is discretized by constructing a set of grid points $x_i = i \Delta x$ and $E_j = j \Delta E$ for some grid spacing defined by Δx and ΔE values being used. For i, j integers, define $u_{i,j} = \phi(x_i, E_j)$, then the transport differential-integral equation (11) can be written in a discrete form as follows, with the starting values $u_{0,j} = 0$ and $v_{0,j} = 0$ being used. For the first step in Δx , approximate the flux by the accumulation of the source over the first interval as

$$u_{1,j} = \Delta x K E_j e^{-E_j/T} \quad (29)$$

followed by the numerical calculation of the rescattering term

$$v_{i,j} = \int_{E_j}^{E_j/\alpha} \frac{\sigma(E') \tau e^{-\tau(E'-E_j)}}{1 - e^{-(1-\alpha)\tau E'}} u(x_i, E') dE' \quad (30)$$

for $i = 1$. After this first, and each successive step, integrals of the type $v_{i,j}$ given by equation (30) are evaluated with Simpson's one-third rule. Evaluate equation (30) for all energies $j = 0, 1, \dots$, and then use a two-step algorithm in a repetitive fashion to advance the solution. For values of α near 1, the numerical solution of equation (11) requires that ΔE become small. The low-energy spectrum then becomes difficult to calculate without special procedures, as cited in reference 17. In this case, a two-step modified Euler predictor-corrector scheme is used (refs. 21 and 22), which is defined by

Second step:

$$\left. \begin{aligned} f_{1,j} &= v_{1,j} + E_j e^{-E_j} - \sigma u_{1,j} \\ u_{2,j} &= \begin{cases} u_{1,j} + \Delta x f_{1,j} & (j=0) \\ \frac{1}{2} (u_{1,j-1} + u_{1,j+1}) + \Delta x f_{1,j} & (j>0) \end{cases} \end{aligned} \right\} \quad (31a)$$

Third step:

$$\left. \begin{aligned} f_{2,j} &= v_{2,j} + E_j e^{-E_j} - \sigma u_{2,j} \\ u_{3,j} &= u_{1,j} + 2\Delta x f_{2,j} \end{aligned} \right\} \quad (31b)$$

The second step is an adoption of the Fredrichs method from reference 21. The third step is a central difference second-order step in Δx . After 100 applications of this two-step algorithm, we apply the following stability correction as suggested in reference 22:

$$\left. \begin{aligned} f_{3,j} &= v_{3,j} + E_j e^{-E_j} - \sigma u_{3,j} \\ u_{3,j} &= \frac{1}{2} (u_{3,j} + u_{2,j}) + \Delta x f_{3,j} \end{aligned} \right\} \quad (32)$$

Note equations (32) are to be understood in an iterative sense and not strictly algebraic sense.

Recursive Solution

In the special case $g(E, x) = g(E)$, a solution to equation (11) is assumed of the form

$$\phi(x, E) = \sum_{n=1}^{\infty} \phi_n(E) f_n(x) = \phi_1(E) f_1(x) + \phi_2(E) f_2(x) + \dots \quad (33)$$

Substitute this series into equation (11) and obtain a solution by requiring that ϕ and f satisfy

$$\left. \begin{aligned} \phi_1(E) &= g(E) \\ \phi_{n+1}(E) &= \int_E^{E/\alpha} f_s(E, E') \phi_n(E') dE' \\ f_1'(x) + \sigma f_1(x) &= 1 \\ f_n'(x) + \sigma f_n(x) &= f_{n-1}(x) \end{aligned} \right\} \quad (34)$$

for $n = 1, 2, 3, \dots$, where the differential equations are subject to the initial condition that $f_n(0) = 0$ for all n . Here the terms for $\phi_n(E)$ are defined recursively and take a great deal of computational time for large values of n . The differential equations have the solutions given by the recursive relations

$$\left. \begin{aligned} f_1(x) &= \frac{1}{\sigma} (1 - e^{-\sigma x}) \\ f_n(x) &= \int_0^x f_{n-1}(u) e^{-\sigma(x-u)} du \end{aligned} \right\} \quad (35)$$

which are easily evaluated for as large a value of n as desired. We find numerically that $|f_n(x)|$ decreases with increasing n for $x < 1$ and increases for $x > 1$ so that the series solution does not converge in this case. For $|x| \leq 1$, we calculated the solution given by equation (35) for terms through $n = 5$ and $n = 6$ and compared them with the numerical solution. The mean values associated with the multigroup method were then adjusted so that the multigroup method agreed with the numerical solution and recursive solution for this special test problem. We then used these same mean values which were associated with numerical source terms as provided by the HZETRN code.

Comparison of Multigroup and Other Solutions

The numerical solutions and recursive solutions of the test problem were then compared with the multigroup solution for neutron penetration in lithium, aluminum, and lead mediums. The results are illustrated in figures 4, 5, and 6. Excellent agreement is obtained in these three cases. In these figures, the solid line represents the numerical solution. The circles represent the recursive solution and the triangles represent the multigroup solution. The various curves were calculated for depths x of 0.1, 0.5, 1.0, 5.0, 10.0, 50.0 and 100.0 g/cm².

The multigroup method has huge advantage in its very short computational time needed to calculate the solution without loss of accuracy. The multigroup method takes less than 1 min of computational time, whereas the Monte Carlo methods require many hours of computational time.

Application for Al-H₂O Shield-Target Configuration

The previous development is now applied to an application of the multigroup method associated with an aluminum-water shield-target configuration. In particular, consider the case where the source term $g(E, x)$ in equation (11) represents evaporation neutrons produced per unit mass per MeV and is specified as a numerical array of values corresponding to various shield-target thicknesses and energies. The numerical array of values is produced by the radiation code HZETRN developed by Wilson et al. (ref. 23). The numerical array of values are actually given in the form $g(E_i, x_j, y_k)$ in units of particles/g-MeV, where y_k represents discrete values for various target thicknesses of water in g/cm², x_j represents discrete values for various shield thicknesses of aluminum, also in units of g/cm², and E_i represents discrete energy values in units of MeV. These discrete source term values are used in the following way. Consider first the solution of equation (11) by the multigroup method for an all-aluminum shield with no target material; i.e., target thickness $y_k = 0$. The HZETRN program was run to simulate the solar particle event of February 23, 1956, and the source term $g(E_i, x_j, y_k)$ associated with an aluminum-water shield was generated for these conditions. With this source term, equation (11) was solved by the multigroup method.

For a single shield material, $\beta = 1$, equation (11) becomes

$$\left[\frac{\partial}{\partial x} + \sigma(E) \right] \phi(x, E) = \int_E^{E/\alpha_1} \sigma_{s1}(E, E') \phi(x, E') dE' + g(E, x) \quad (36)$$

where an integration of equation (36) from E_i to E_{i+1} produces

$$\begin{aligned} \int_{E_i}^{E_{i+1}} \frac{\partial \phi}{\partial x} dE + \int_{E_i}^{E_{i+1}} \sigma(E) \phi(x, E) dE \\ = \int_{E_i}^{E_{i+1}} \int_E^{E/\alpha_1} \sigma_{s1}(E, E') \phi(x, E') dE' dE + \int_{E_i}^{E_{i+1}} g(E, x) dE \end{aligned} \quad (37)$$

We define the quantities

$$\left. \begin{aligned} \Phi_i &= \int_{E_i}^{E_{i+1}} \phi(x, E) dE \\ b_i &= \int_{E_i}^{E_{i+1}} g(E, x) dE \end{aligned} \right\} \quad (38)$$

and interchange the order of integration of the double integral terms in equation (37). Then apply the mean value theorem to obtain the result

$$\begin{aligned} \frac{d\Phi_i}{dx} + \bar{\sigma}\Phi_i = & \int_{E_i}^{E_{i+1}} \int_{E=E_i}^{E'} \sigma_{s_1}(E, E') dE \phi(x, E') dE' \\ & + \int_{E_{i+1}}^{E_{i+2}} \int_{E=\alpha_1 E'}^{E_{i+1}} \sigma_{s_1}(E, E') dE \phi(x, E') dE' + b_i \end{aligned} \quad (39)$$

over the energy group $E_i < E' < E_{i+1}$. For the energy spacing $E_{i+1} = E_i/\alpha$, the first double integral in equation (39) represents integration over the lower triangle illustrated in figure 2(c). The second double integral in equation (39) represents integration over the upper triangle illustrated in figure 2(c). Define

$$\left. \begin{aligned} g_1(E') &= \int_{E=E_i}^{E'} \sigma_{s_1}(E, E') dE \\ g_2(E') &= \int_{E=\alpha_1 E'}^{E_{i+1}} \sigma_{s_1}(E, E') dE \end{aligned} \right\} \quad (40)$$

and then employ another application of a mean value theorem for integrals to write equation (39) in the form

$$\frac{d\Phi_i}{dx} + \bar{\sigma}\Phi_i = g_1[E_i + \theta_1(E_{i+1} - E_i)]\Phi_i + g_2[E_{i+1} + \theta_2(E_{i+2} - E_{i+1})]\Phi_{i+1} + b_i \quad (41)$$

This produces the coefficients associated with the energy group E_i to E_{i+1} , which are given by

$$\left. \begin{aligned} a_{ii} &= g_1 - \bar{\sigma} \\ a_{i,i+1} &= g_2 \end{aligned} \right\} \quad (42)$$

In this way, the diagonal and off-diagonal elements of the coefficient matrix in equation (26) are calculated.

For a compound target material, comprised of material 1 and material 2, there are two values of α . A value α_1 is selected for material 1 and a value α_2 is selected for material 2 of the compound material. In this case, equation (36) takes on the form

$$\begin{aligned} \left[\frac{\partial}{\partial x} + \sigma(E) \right] \phi(x, E) = & \int_E^{E/\alpha_1} \sigma_{s_1}(E, E') \phi(x, E') dE' \\ & + \int_E^{E/\alpha_2} \sigma_{s_2}(E, E') \phi(x, E') dE' + g(E, x) \end{aligned} \quad (43)$$

where σ_{s_1} and σ_{s_2} are scattering terms associated with the respective materials. These terms are calculated in the HZETRN code. Two cases are considered. The first case requires that the E/α_2 line be above the E/α_1 line. (See fig. 2(d).) The second case is where $\alpha_2 = 0$ (the hydrogen case) and the limits of integration for the second integral goes to infinity. Each case is considered separately.

For the first case, assume that $\alpha_1 > \alpha_2 > 0$ and select the exact energy spacing dictated by the E/α_2 line. Then proceed as for the single shield material. Integrate equation (43)

from E_i to E_{i+1} and interchange the order of integration on the double integral terms. Define $b_i = \int_{E_i}^{E_{i+1}} g(E, x) dE$ and obtain the equation

$$\frac{d\Phi_i}{dx} + \bar{\sigma}\Phi_i = I_{11} + I_{12} + I_{21} + I_{22} + b_i \quad (44)$$

where now the I_{21} and I_{22} integrals have, because of the exact spacings, the forms

$$\left. \begin{aligned} I_{21} &= \int_{E_i}^{E_{i+1}} \int_{E=E_i}^{E'} \sigma_{s2}(E, E') dE \phi(x, E') dE' \\ I_{22} &= \int_{E_{i+1}}^{E_{i+2}} \int_{E=\alpha_2 E'}^{E_{i+1}} \sigma_{s2}(E, E') dE \phi(x, E') dE' \end{aligned} \right\} \quad (45)$$

Defining the terms

$$\begin{aligned} h_{1(i)}(E') &= \int_{E=E_i}^{E'} \sigma_{s_i}(E, E') dE \quad (i = 1, 2) \\ h_{2(i)}(E') &= \int_{E=\alpha_2 E'}^{E_{i+1}} \sigma_{s_i}(E, E') dE \quad (i = 1, 2) \end{aligned}$$

and using the mean value theorem for integrals gives from equations (45)

$$I_{21} = h_{1(2)}[E_i + \theta_1(E_{i+1} - E_i)]\Phi_i$$

and

$$I_{22} = h_{2(2)}[E_{i+1} + \theta_2(E_{i+2} - E_{i+1})]\Phi_{i+1}$$

where θ_1 and θ_2 define intermediate energy values associated with the mean value theorem. The integrals I_{11} and I_{12} are associated with integration limits $(E, E/\alpha_1)$ and energy intervals dictated by the selection of α_2 for determining the exact energy spacings. These integrals are associated with the trapezoidal area 1 (A1) and triangular area 2 (A2) illustrated in figure 2(d). These areas are a fraction of the triangle areas associated with the line $E' = E/\alpha_2$. These fractions are given by

$$\left. \begin{aligned} f_1 &= \frac{\frac{1}{2}(E_{i+1} - E_i)^2 - \frac{1}{2}(E_{i+1} - E_i/\alpha_1)(E_{i+1} - \alpha_1 E_{i+1})}{\frac{1}{2}(E_{i+1} - E_{i+1}/\alpha_2)^2} \\ f_2 &= \frac{(E_{i+1}/\alpha_1 - E_{i+1})(E_{i+1} - \alpha_1 E_{i+1})}{(E_{i+1} - E_i)(E_{i+2} - E_{i+1})} \end{aligned} \right\} \quad (46)$$

and we write

$$\left. \begin{aligned} I_{11} &= f_1 h_{1(1)} \Phi_i \\ I_{12} &= f_2 h_{2(1)} \Phi_{i+1} \end{aligned} \right\} \quad (47)$$

The coefficients for the system of differential equations in equation (27) are then given by

$$\left. \begin{aligned} a_{11} &= h_{1(2)} + f_1 h_{1(1)} - \bar{\sigma} \\ a_{12} &= h_{2(2)} + f_2 h_{2(1)} \end{aligned} \right\} \quad (48)$$

For the second case, of hydrogen, α_2 equals 0; therefore one of the limits of integration becomes infinite. Let α_1 determine the energy spacing in this case. Again integrate equations (45) over the energy interval (E_i, E_{i+1}) , which is determined by the $E' = E/\alpha_1$ line. With the definitions given by equations (38), integrate equation (43) over the interval (E_i, E_{i+1}) and then interchange the order of integration in the resulting double integrals to obtain

$$\frac{d\Phi_i}{dx} + \bar{\sigma}\Phi_i = I_1^* + I_2^* + b_i$$

where

$$I_1^* = \int_{E_i}^{E_{i+1}} \int_{E=E_i}^{E'} \sigma_{s1}(E, E') dE \phi(x, E') dE' + \int_{E_{i+1}}^{E_{i+2}} \int_{E=\alpha_1 E'}^{E_{i+1}} \sigma_{s1}(E, E') dE \phi(x, E') dE'$$

and

$$I_2^* = \int_{E_i}^{E_{i+1}} \int_{E_i}^{E'} \sigma_{s2}(E, E') dE \phi(x, E') dE' + \sum_{j=1}^N \int_{E_{i+j}}^{E_{i+j+1}} \int_{E_i}^{E_{i+1}} \sigma_{s2}(E, E') dE \phi(x, E') dE'$$

and for all N^* greater than some integer $N > 0$, it is known that $\phi(x, E)$ will be zero. Define

$$\begin{aligned} h_3(E') &= \int_{E_i}^{E'} \sigma_{s1}(E, E') dE & (E_i < E' < E_{i+1}) \\ h_4(E') &= \int_{\alpha_1 E'}^{E_{i+1}} \sigma_{s1}(E, E') dE & (E_{i+1} < E' < E_{i+2}) \\ h_5(E') &= \int_{E_i}^{E'} \sigma_{s2}(E, E') dE & (E_i < E' < E_{i+1}) \\ h_{6(j)} &= \int_{E_{i+j}}^{E_{i+j+1}} \sigma_{s2}(E, E') dE & (E_{i+j} < E' < E_{i+j+1}) \end{aligned}$$

and then write the coefficients associated with the system of differential equations as

$$\begin{aligned} a_{i,i} &= h_3 + h_5 - \bar{\sigma} \\ a_{i,i+1} &= h_4 + h_{6(1)} \\ a_{i,i+2} &= h_{6(2)} \\ a_{i,i+3} &= h_{6(3)} \\ &\vdots \\ a_{i,i+n} &= h_{6(n)} \end{aligned}$$

In this way a system of equations is generated that has the triangular form given by the system of equations in equation (27).

Again use the source term $g(E_i, x_j, y_k)$ obtained from the HZETRN simulation of the solar particle event of February 23, 1956, associated with an aluminum-water shield-target configuration. Note that now the multigroup system of equations (eq. (27)) associated with equation (39) must be solved for the multiple atom target material of water. Consider the cases of discrete shield thickness x_2, x_3, \dots and apply the multigroup method to the solution of

equation (11) applied to all target material $y > 0$. For each value of x_i considered, the initial conditions are obtained from the previous solutions generated where $y = 0$. This represents the application of the multigroup method to two different regions: region 1 of all shield material and region 2 of all target material. Then continue to apply the multigroup method to region 2 for each discrete value of shield thickness, where the initial conditions on the start of the second region represents exit conditions from the shield region 1. This provides for continuity of the solutions for the fluence between the two regions.

Results and Discussion

The present formalism was used to evaluate the neutron fluence for various aluminum shield and water target combinations. Figure 7 illustrates the low-energy neutron fluence due to the scattering of evaporation neutrons in an aluminum shield for various thicknesses with $y_k = 0$ (i.e., no target material). Figure 8 illustrates the total neutron fluence for various aluminum shield thicknesses. This fluence consists of the HZETRN-generated neutron fluence plus the multigroup-generated low-energy neutron fluence. Figures 9, 10, and 11 are graphs of the neutron fluence in depths of 1, 10, and 100 g/cm² of aluminum generated from the HZETRN code both with and without the addition of the multigroup evaporation neutrons.

Typical results for no shield before the water target are illustrated in figures 12, 13, and 14 where a comparison of the multigroup method with the previous HZETRN results for thicknesses of 1, 10, and 30 g/cm² can be made. Note that in the calculations of the multigroup method, the source terms $g(E, x)$, the scattering term $\sigma_s(E, E')$, and cross section $\sigma(E)$ of equation (11) are all given as numerical output from the HZETRN code for the solar particle event of February 23, 1956. Also note that these calculations were compared with the LAHET Monte Carlo results from reference 24. Figures 12, 13, and 14 illustrate this comparison for neutron fluences versus energy at water depths of 1, 10, and 30 g/cm², respectively. Figure 15 is a graph of neutron fluence versus depth in a shield-target configuration of 100 g/cm² of aluminum followed by 100 g/cm² of water. Observe the increase in the low-energy neutron fluence at the aluminum-water boundary. This increase is caused by high-energy neutrons colliding with hydrogen atoms, which results in large energy losses. In these types of collisions, the neutrons of modest energies give up one half of their energy on the average; thus, the lower energy neutron fluence is increased.

In figures 12, 13, and 14, note the distinct improvement of the fluence by using the multigroup evaporation neutrons over that of the previous HZETRN results. These improved results are still a little lower than the results predicted by the Monte Carlo simulation. These figures show that the multigroup method is more accurate at the higher target depths compared with results at the lower depths. This is due to the straight-ahead approximation assumptions used in the one-dimensional Boltzmann equation, where all secondaries produced by nuclear collisions are assumed to move in the same direction as the primary nucleon which caused the collision. This assumption is true for secondaries which are high-energy particles. This straight-ahead approximation is not true for low-energy neutrons produced by evaporation because these neutrons are generally isotropically distributed. These neutrons make up the source terms in the multigroup method. The straight-ahead assumption causes errors at the smaller target depths because it fails to account for all the low-energy neutrons transported back from larger depths of the material. In an attempt to improve the performance of the multigroup method for simulating low-energy neutrons, the assumption was made that only one half the source terms moved in the forward direction while the other half moved in the backward direction. The solution of the multigroup system of equations (eq. (27)) was then modified. Using one half the source terms $g(E_i, x_j, y_k)$, system of equations (eq. (27)) was marched first through the shield material and then through the target material. By using the end boundary condition generated, the equations were then marched backwards through the target and then the shield material. The fluences from the forward and backward marching were then added to obtain a total fluence. This process

is referred to in the figures as the two-dimensional multigroup method. Figures 16, 17, and 18 illustrate the results of the two-directional multigroup method applied to the case of no shield and a target of water only for nominal depths for an exposure to the solar particle event of February 23, 1956. Figure 19 illustrates the fluence in a depth of 10 g/cm² of water when the two-dimensional method was applied to a 100 g/cm² aluminum shield followed by a 100 g/cm² target of water when exposed to the solar particle event of February 23, 1956. Observe that the two-directional multigroup method greatly improves the low-energy fluence predictions at the smaller depths.

Research is continuing to close the remaining gap between transport code predictions and Monte Carlo results. Possible errors from various sources are being investigated. The nuclear cross sections used are believed to be one source of error because only elastic cross sections were used in the multigroup simulation. The elastic cross sections are much larger than the nonelastic cross sections at low energies. Nonelastic cascading does occur and it is believed that the multigroup method would be improved by incorporating both types of cross sections. Other sources of errors reside in the HZETRN program itself. The nuclear cross sections used by HZETRN are interpolated from a large database that was developed experimentally many years ago; this database needs to be updated. The HZETRN code is a one-dimensional transport code using the straight-ahead approximation. The improvement of the multigroup method in going from the straight-ahead approximation to the two-directional multigroup approximation suggests that similar type changes be incorporated into the HZETRN code in order to reflect the nonisotropic character of the events.

Concluding Remarks

These preliminary studies have shown that the multigroup method developed for the study of low-energy neutron transport has made significant improvements in and is compatible with the current HZETRN code developed at Langley Research Center. It has proven to be a fast and efficient algorithm for the inclusion of low-energy neutrons into the HZETRN code. The addition of nonelastic processes in the low-energy neutron transport is expected to further improve the result.

References

1. Wilson, John W.; Cucinotta, F. A.; Shinn, J. L.; Simonsen, L. C.; Dubey, R. R.; Jordan, W. R.; Jones, T. D.; Chang, C. K.; and Kim, M. Y.: Shielding From Solar Particle Event Exposures in Deep Space. *Rad. Meas.*, vol. 30, 1999, pp. 361–382.
2. Wilson, J. W.; Cucinotta, F. A.; and Simonsen, L. C.: Proton Target Fragmentation Effects in Space Exposures. *Adv. Space Res.*, To be published.
3. Wilson, John W.; Nealy, John E.; Wood, James S.; Qualls, Garry D.; Atwell, William; Shinn, Judy L.; and Simonsen, Lisa C.: Variations in Astronaut Radiation Exposure Due to Anisotropic Shield Distribution. *Health Phys.*, vol. 69, no. 1, 1995, pp. 34–45.
4. Nealy, John E.; Qualls, Garry D.; and Simonsen, Lisa C.: Integrated Shield Design Methodology: Application to a Satellite Instrument. *Shielding Strategies for Human Space Exploration*, J. W. Wilson, J. Miller, A. Konradi, and F. A. Cucinotta, eds., NASA CP-3360, 1997, pp. 383–396.
5. Wilson, John W.; Cucinotta, F. A.; Shinn, J. L.; Simonsen, L. C.; and Badavi, F. F.: *Overview of HZETRN and BRNTRN Space Radiation Shielding Codes*. SPIE Paper No. 2811-08, 1996.
6. Alsmiller, R. G., Jr.; Irving, D. C.; Kinney, W. E.; and Moran, H. S.: The Validity of the Straightahead Approximation in Space Vehicle Shielding Studies. *Second Symposium on Protection Against Radiations in Space*, Arthur Reetz, Jr., ed., NASA SP-71, 1965, pp. 177–186.
7. Wilson, John W.; and Khandelwal, G. S.: Proton Dose Approximation in Arbitrary Convex Geometry. *Nucl. Technol.*, vol. 23, no. 3, Sept. 1974, pp. 298–305.
8. Wilson, John W.; and Lamkin, Stanley L.: Perturbation Theory for Charged-Particle Transport in One Dimension. *Nucl. Sci. & Eng.*, vol. 57, no. 4, Aug. 1975, pp. 292–299.

9. Lamkin, Stanley Lee: A Theory for High-Energy Nucleon Transport in One Dimension. M.S. Thesis, Old Dominion Univ., Dec. 1974.
10. Letaw, John; Tsao, C. H.; and Silberberg, R.: Matrix Methods of Cosmic Ray Propagation. *Composition and Origin of Cosmic Rays*, Maurice M. Shapiro, ed., D. Reiel Publ. Co., 1983, pp. 337–342.
11. Wilson, John W.: *Analysis of the Theory of High-Energy Ion Transport*. NASA TN D-8381, 1977.
12. Wilson, John W.; and Badawi, F. F.: Methods of Galactic Heavy Ion Transport. *Radiat. Res.*, vol. 108, 1986, pp. 231–237.
13. Wilson, John W.; Townsend, Lawrence W.; Nealy, John E.; Chun, Sang Y.; Hong, B. S.; Buck, Warren W.; Lamkin, S. L.; Ganapol, Barry D.; Khan, Ferdous; and Cucinotta, Francis A.: *BRYNTRN: A Baryon Transport Model*. NASA TP-2887, 1989.
14. Shinn, Judy L.; Wilson, John W.; Nealy, John E.; and Cucinotta, Francis A.: *Comparison of Dose Estimates Using the Buildup-Factor Method and a Baryon Transport Code (BRYNTRN) With Monte Carlo Results*. NASA TP-3021, 1990.
15. Lamkin, Stanley L.; Khandelwal, Govind S.; Shinn, Judy L.; and Wilson, John W.: Space Proton Transport in One Dimension. *Nucl. Sci. & Eng.*, vol. 116, no. 4, 1994, pp. 291–299.
16. Shinn, Judy L.; Wilson, John W.; Lone, M. A.; Wong, P. Y.; and Costen, Robert C.: *Preliminary Estimates of Nucleon Fluxes in a Water Target Exposed to Solar-Flare Protons: BRYNTRN Versus Monte Carlo Code*. NASA TM-4565, 1994.
17. Wilson, John W.; Townsend, Lawrence W.; Schimmerling, Walter S.; Khandelwal, Govind S.; Khan, Ferdous S.; Nealy, John E.; Cucinotta, Francis A.; Simonsen, Lisa C.; Shinn, Judy L.; and Norbury, John W.: *Transport Methods and Interactions for Space Radiations*. NASA RP-1257, 1991.
18. Haffner, James W.: *Radiation and Shielding in Space*. Academic Press, 1967.
19. Brookhaven Nat. Lab.: *Guidebook for the ENDF/B-V Nuclear Data Files*. EPRI NP-2510, Electric Power Res. Inst., 1982.
20. Cloudsley, Martha Sue: A Numerical Solution of the Low Energy Neutron Boltzmann Equation. Ph.D. Thesis, Old Dominion University, May 1999.
21. Hall, Charles A.; and Porsching, Thomas A.: *Numerical Analysis of Partial Differential Equations*. Prentice Hall, 1990.
22. Dahlquist, Germund; and Björck, Åke: *Numerical Methods*. Prentice Hall, 1974.
23. Wilson, John W.; Badawi, Francis F.; Cucinotta, Francis A.; Shinn, Judy L.; Badhwar, Gautam D.; Silberberg, R.; Tsao, C. H.; Townsend, Lawrence W.; and Tripathi, Ram K.: *HZETRN: Description of Free-Space Ion and Nucleon Transport and Shielding Computer Program*. NASA TP-3495, 1995.
24. Prael, R. E.; and Lichtenstein, Henry: *User Guide to LCS: The LAHET Code System*. LA-UR-89-3014, Los Alamos Nat. Lab., 1989.

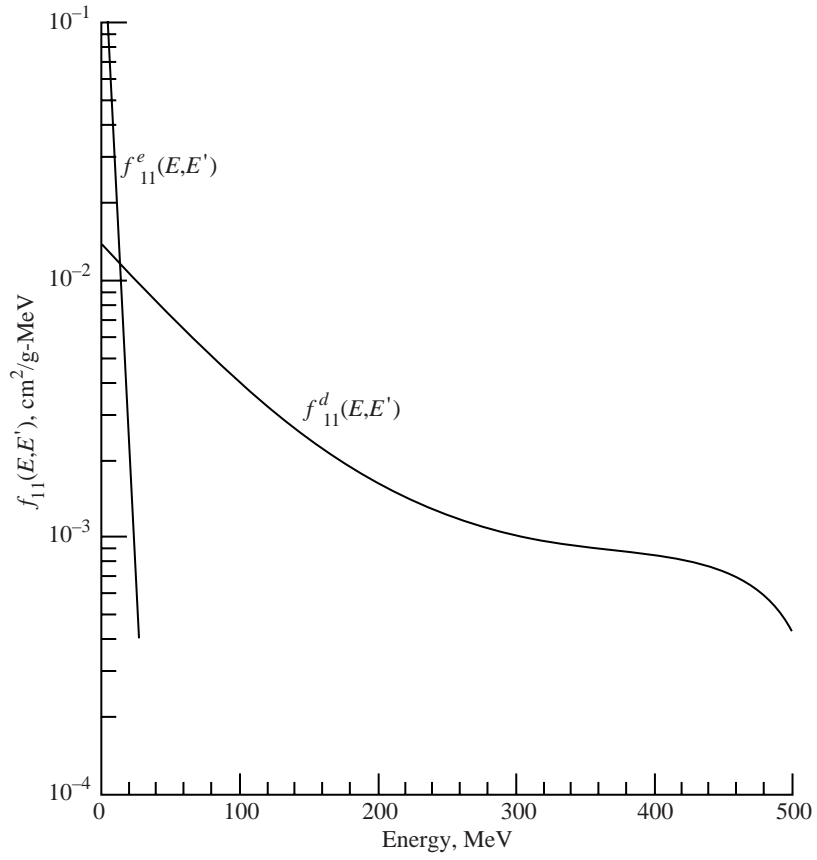
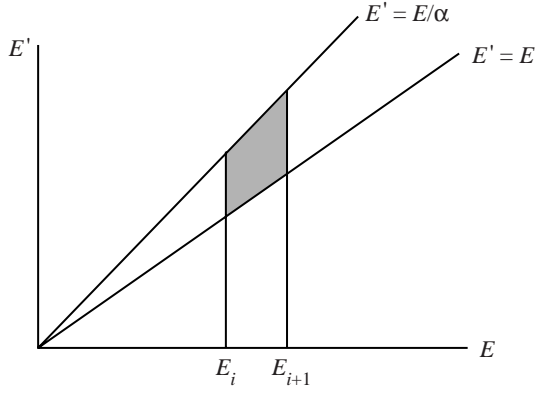
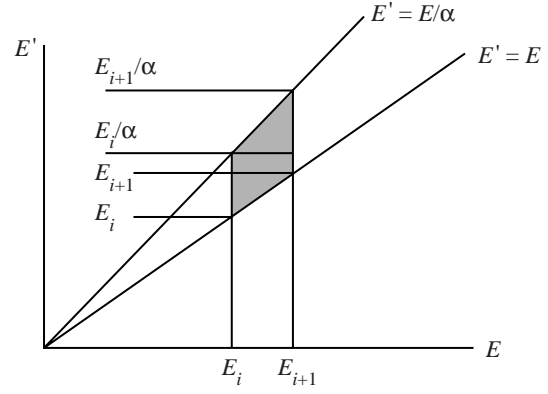


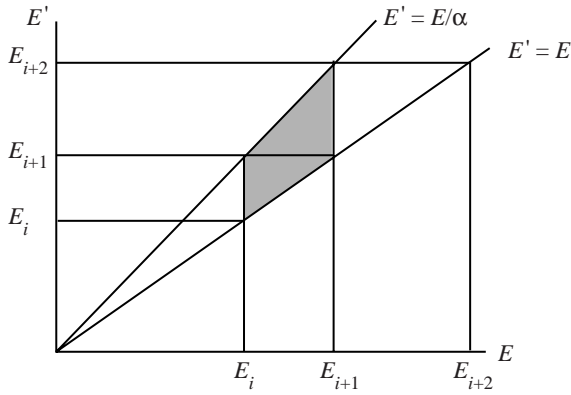
Figure 1. Evaporation and cascading neutron spectral effects for collision of 500 MeV neutrons in aluminum.



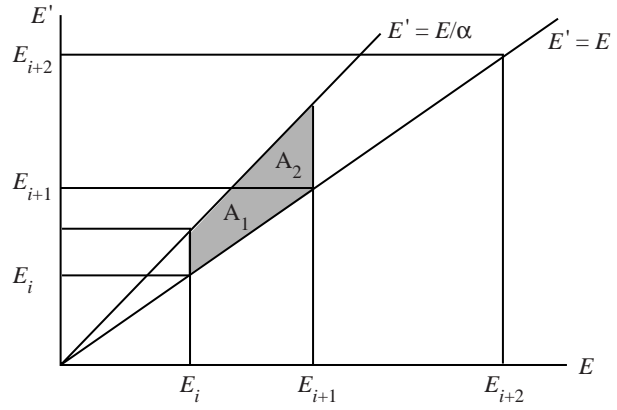
(a) General.



(b) $E_{i+1} < \frac{E_i}{\alpha}$.



(c) $E_{i+1} = \frac{E_i}{\alpha}$



(d) $E_{i+1} > \frac{E_i}{\alpha}$.

Figure 2. Various energy partitioning schemes.

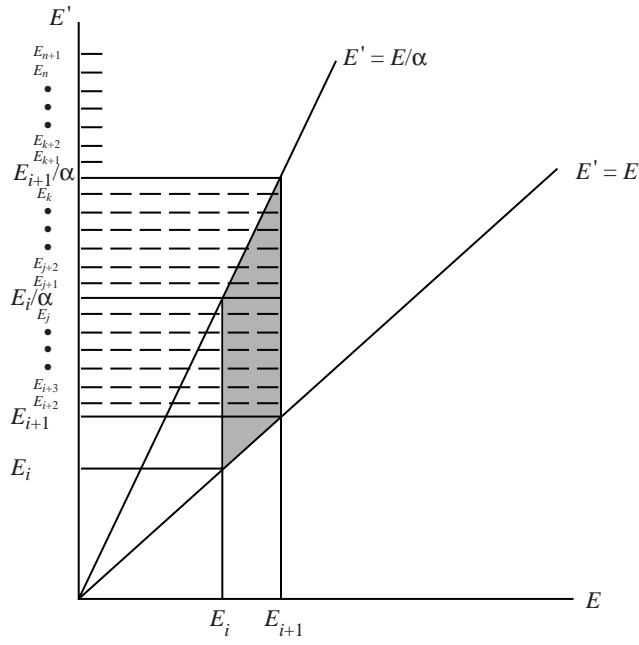


Figure 3. Multigroup energy partition where $E_{i+1} < \frac{E_i}{\alpha}$.

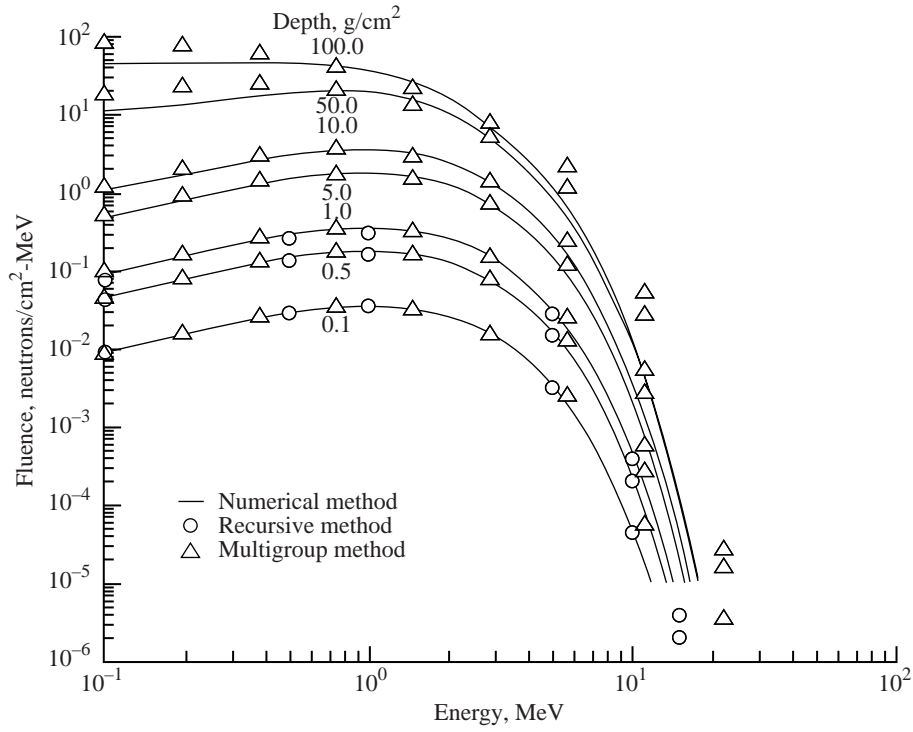


Figure 4. Numerical and multigroup solutions for lithium.

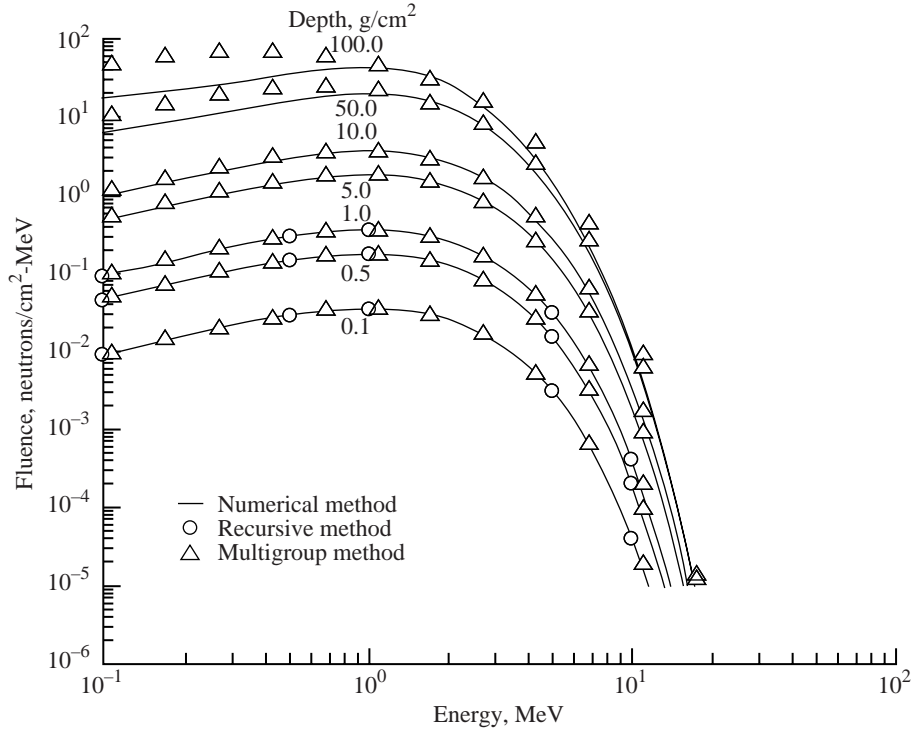


Figure 5. Numerical solution and multigroup solution for aluminum.

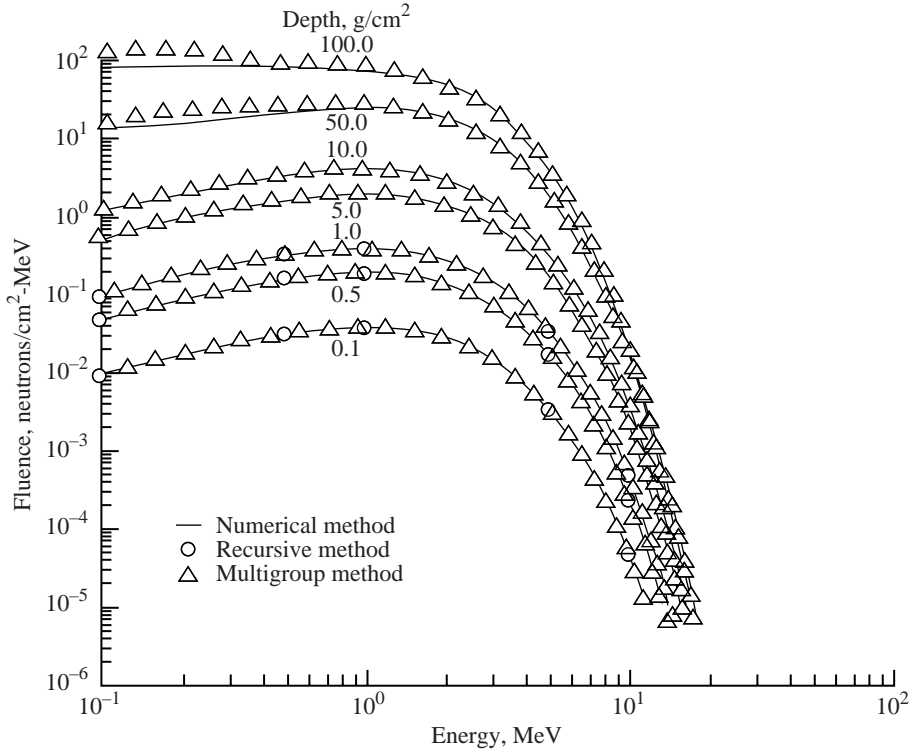


Figure 6. Numerical solution and multigroup solution for lead.

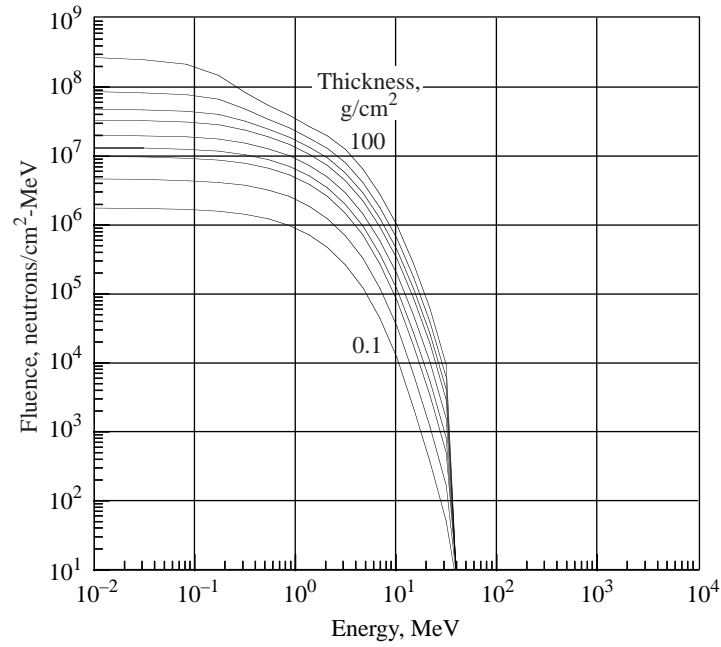


Figure 7. Low-energy neutron fluences due to scattering of evaporation neutrons in aluminum shield exposed to solar particle event of February 23, 1956.

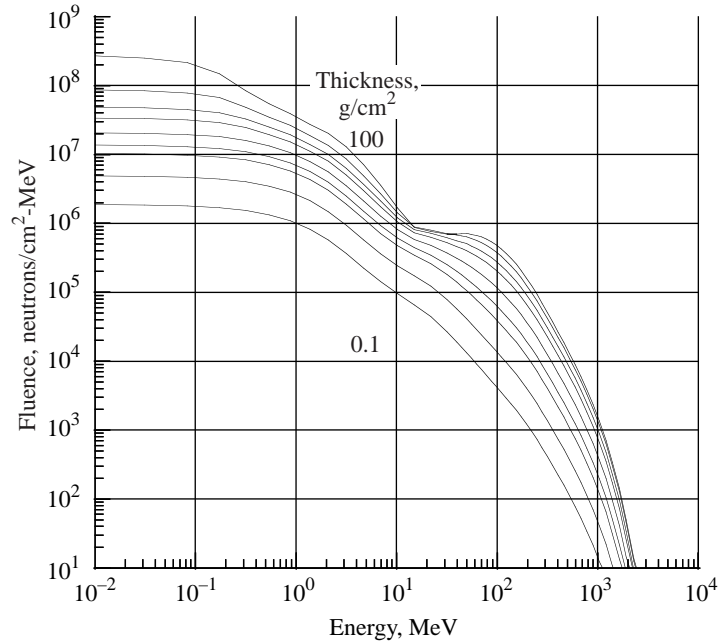


Figure 8. Total neutron fluences in aluminum shield exposed to solar particle event of February 23, 1956.

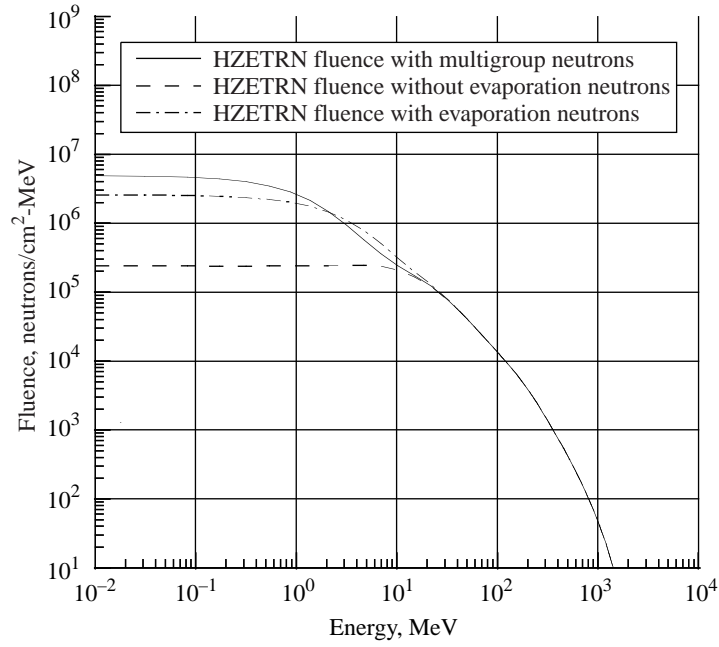


Figure 9. Energy spectra of neutron fluence at depth of 1 g/cm^2 in aluminum exposed to solar particle event of February 23, 1956.

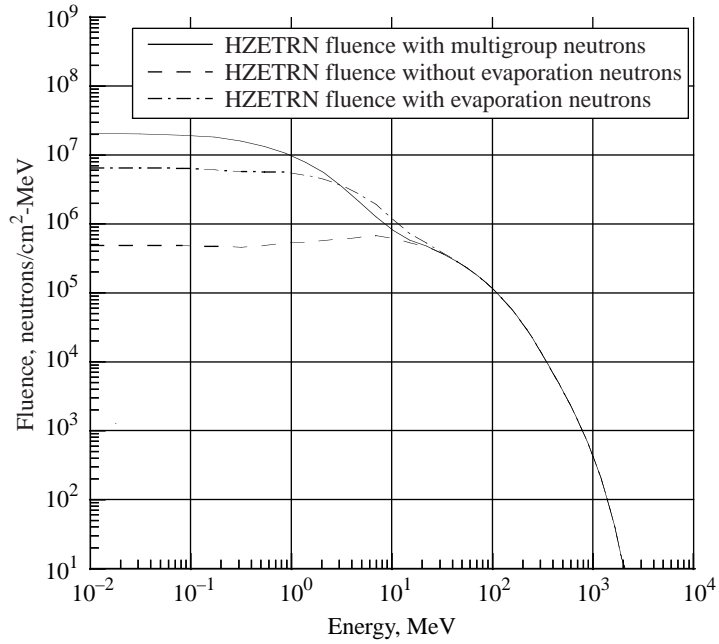


Figure 10. Energy spectra of neutron fluence at depth of 10 g/cm^2 in aluminum exposed to solar particle event of February 23, 1956.

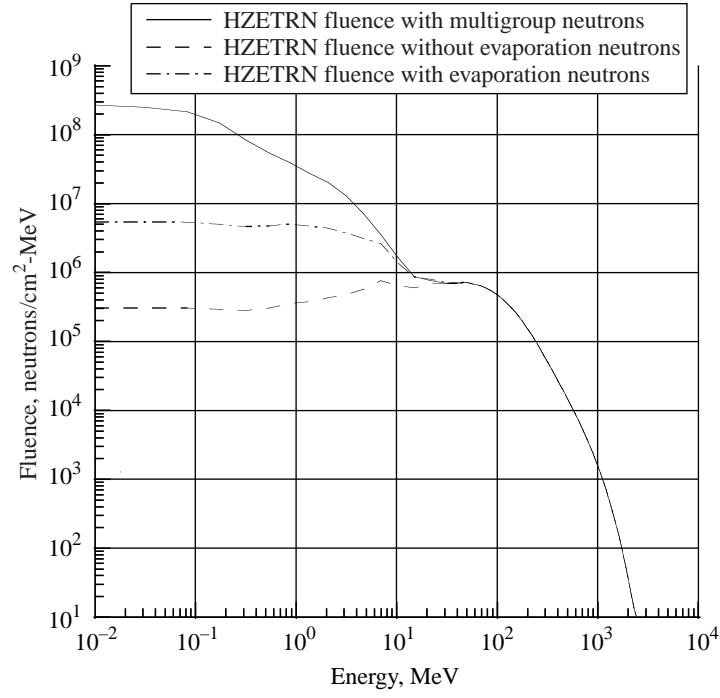


Figure 11. Energy spectra of neutron fluence at depth of 100 g/cm² in aluminum exposed to solar particle event of February 23, 1956.

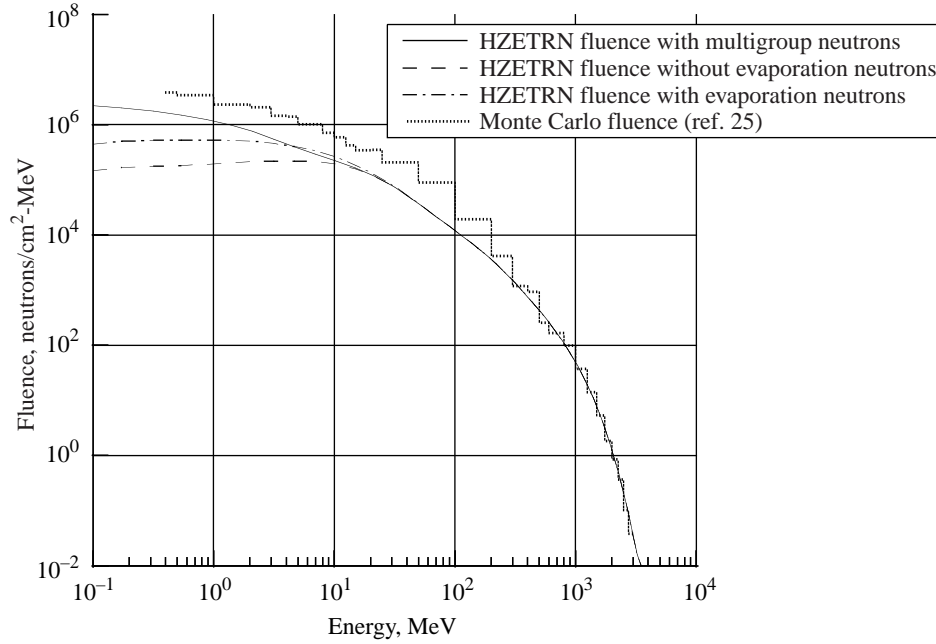


Figure 12. Energy spectra of neutron fluence at depth of 1 g/cm² in water exposed to solar particle event of February 23, 1956.

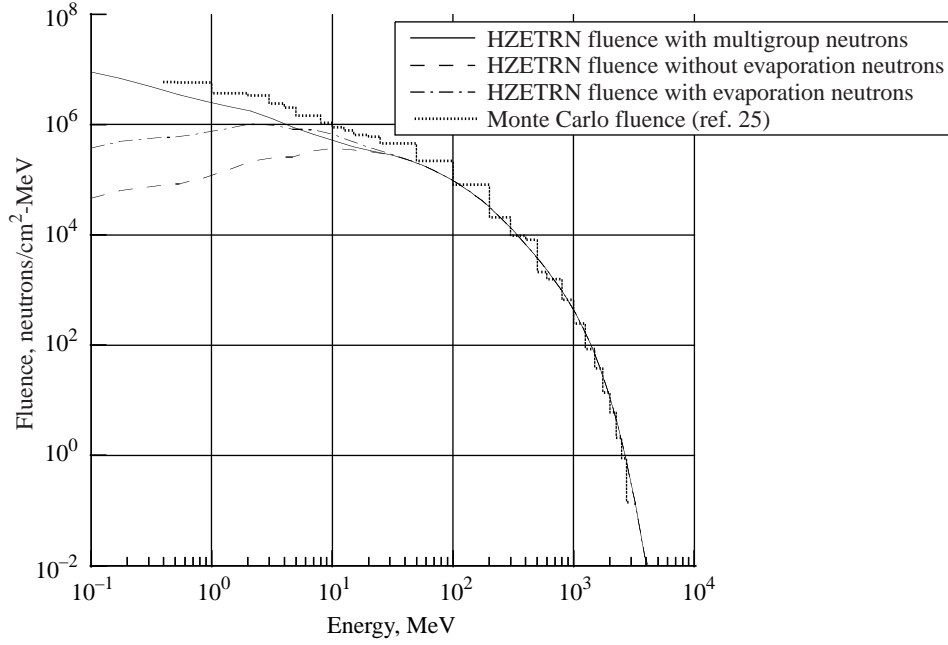


Figure 13. Energy spectra of neutron fluence at depth of 10 g/cm² in water exposed to solar particle event of February 23, 1956.

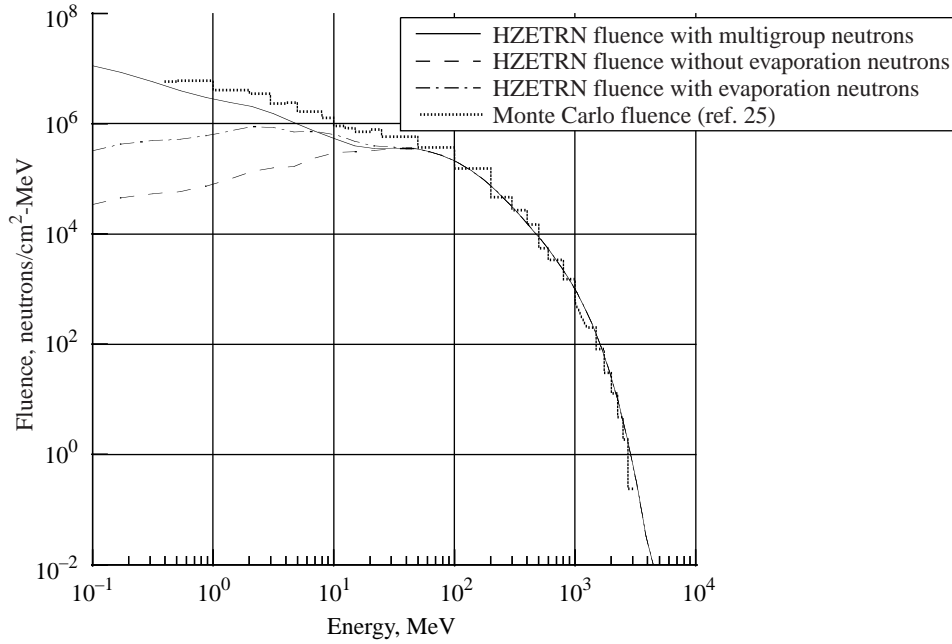


Figure 14. Energy spectra of neutron fluence at depth of 30 g/cm² in water exposed to solar particle event of February 23, 1956.

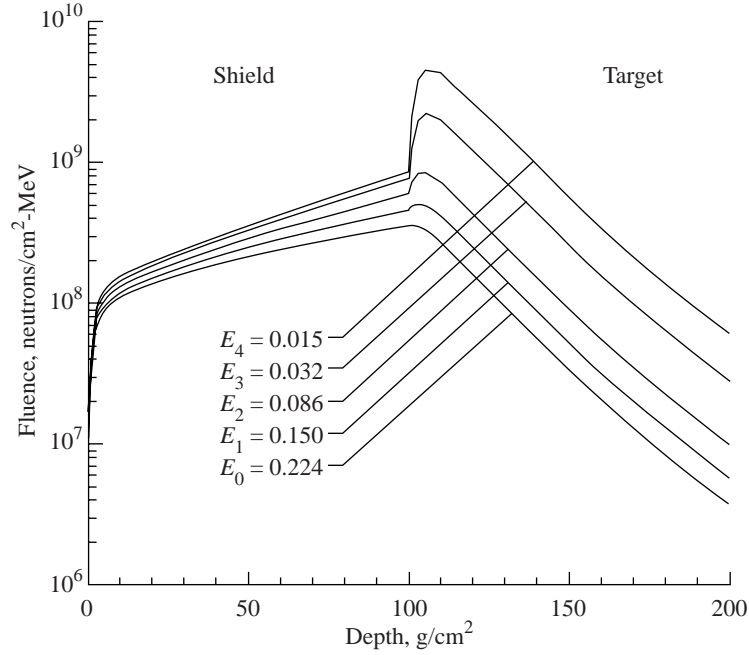


Figure 15. Neutron fluence as function of depth in 100 g/cm² aluminum shield followed by 100 g/cm² water target.

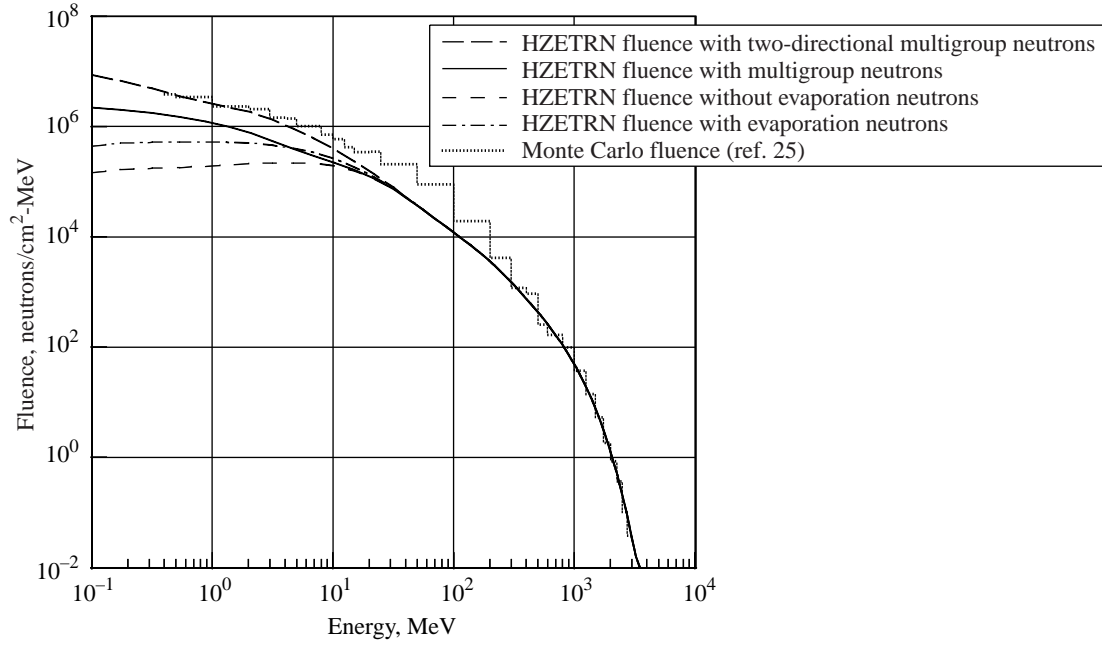


Figure 16. Energy spectra of neutron fluence at depth of 1 g/cm² in water exposed to solar particle event of February 23, 1956, and calculated with two-directional multigroup method.

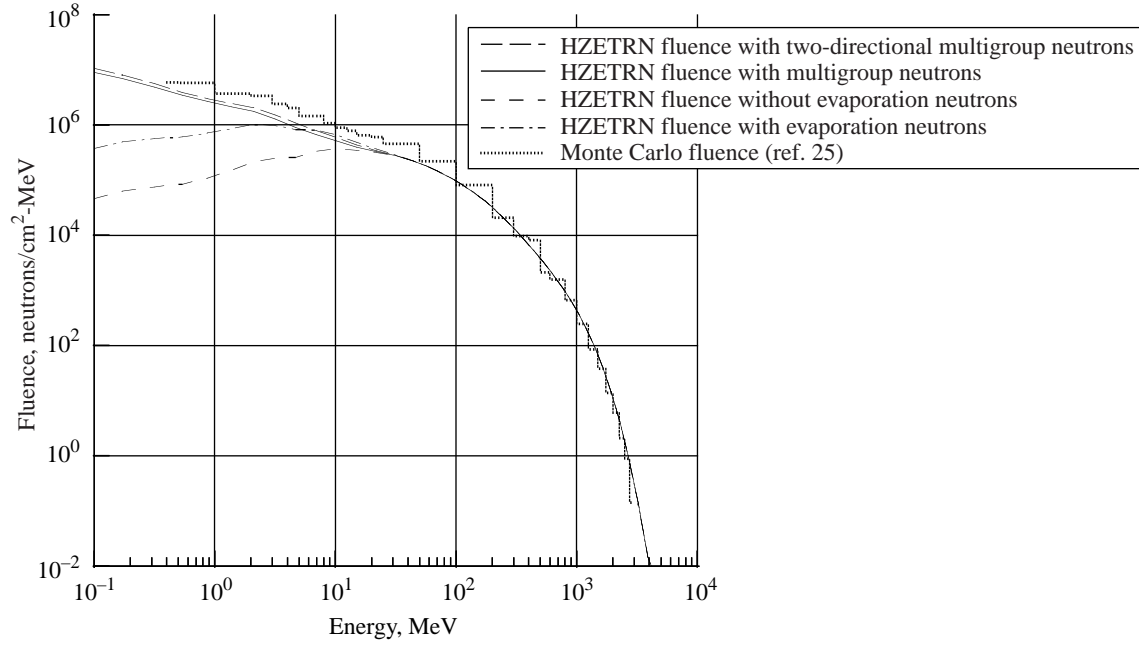


Figure 17. Energy spectra of neutron fluence at depth of 10 g/cm^2 in water exposed to solar particle event of February 23, 1956, and calculated with two-directional multigroup method.

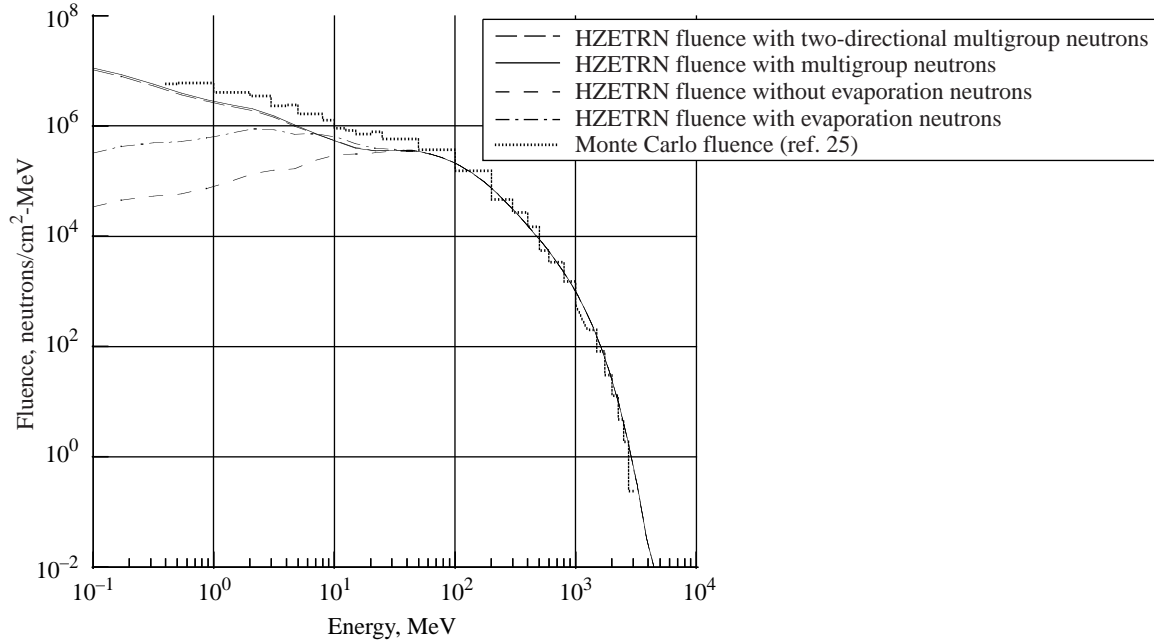


Figure 18. Energy spectra of neutron fluence at depth of 30 g/cm^2 in water exposed to solar particle event of February 23, 1956, and calculated with two-directional multigroup method.

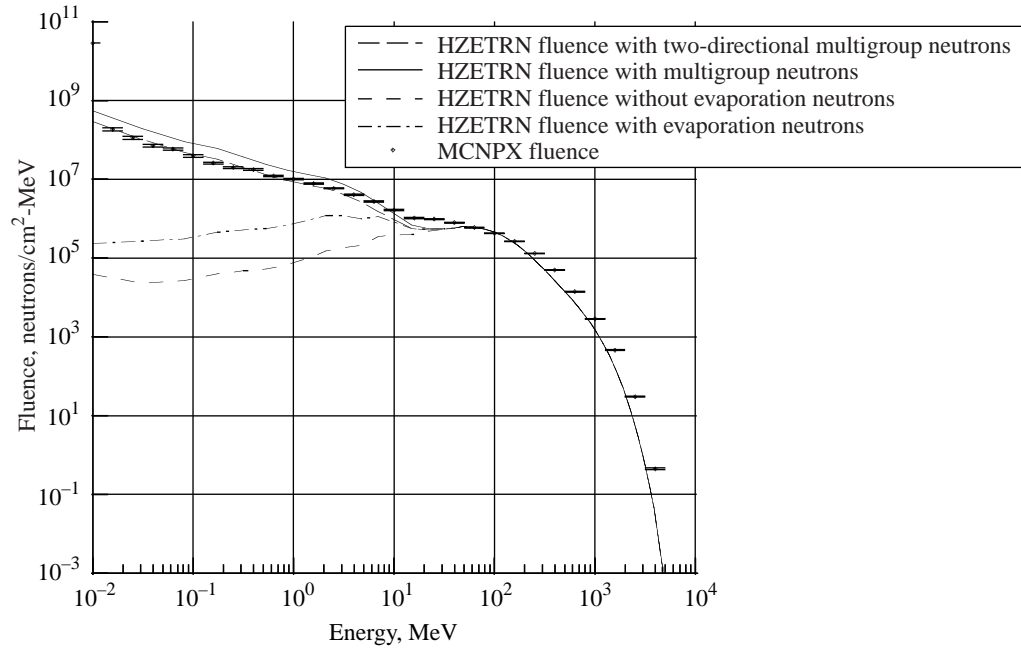


Figure 19. Energy spectra of neutron fluence at depth of 10 g/cm² in target of 100 g/cm² aluminum shield with target of 100 g/cm² of water behind it when exposed to solar particle event of February 23, 1956, and calculated with two-directional multigroup method.

REPORT DOCUMENTATION PAGE			Form Approved OMB No. 0704-0188	
Public reporting burden for this collection of information is estimated to average 1 hour per response, including the time for reviewing instructions, searching existing data sources, gathering and maintaining the data needed, and completing and reviewing the collection of information. Send comments regarding this burden estimate or any other aspect of this collection of information, including suggestions for reducing this burden, to Washington Headquarters Services, Directorate for Information Operations and Reports, 1215 Jefferson Davis Highway, Suite 1204, Arlington, VA 22202-4302, and to the Office of Management and Budget, Paperwork Reduction Project (0704-0188), Washington, DC 20503.				
1. AGENCY USE ONLY (Leave blank)	2. REPORT DATE March 2000	3. REPORT TYPE AND DATES COVERED Technical Publication		
4. TITLE AND SUBTITLE An Improved Neutron Transport Algorithm for Space Radiation		5. FUNDING NUMBERS WU 101-15-01-51		
6. AUTHOR(S) John H. Heinbockel, Martha S. Cloudsley, and John W. Wilson				
7. PERFORMING ORGANIZATION NAME(S) AND ADDRESS(ES) NASA Langley Research Center Hampton, VA 23681-2199		8. PERFORMING ORGANIZATION REPORT NUMBER L-17876		
9. SPONSORING/MONITORING AGENCY NAME(S) AND ADDRESS(ES) National Aeronautics and Space Administration Washington, DC 20546-0001		10. SPONSORING/MONITORING AGENCY REPORT NUMBER NASA/TP-2000-209865		
11. SUPPLEMENTARY NOTES Heinbockel and Cloudsley: Old Dominion University, Norfolk, VA; Wilson: Langley Research Center, Hampton, VA.				
12a. DISTRIBUTION/AVAILABILITY STATEMENT Unclassified-Unlimited Subject Category 93 Distribution: Standard Availability: NASA CASI (301) 621-0390		12b. DISTRIBUTION CODE		
13. ABSTRACT (Maximum 200 words) A low-energy neutron transport algorithm for use in space radiation protection is developed. The algorithm is based upon a multigroup analysis of the straight-ahead Boltzmann equation by using a mean value theorem for integrals. This analysis is accomplished by solving a realistic but simplified neutron transport test problem. The test problem is analyzed by using numerical and analytical procedures to obtain an accurate solution within specified error bounds. Results from the test problem are then used for determining mean values associated with rescattering terms that are associated with a multigroup solution of the straight-ahead Boltzmann equation. The algorithm is then coupled to the Langley HZETRN code through the evaporation source term. Evaluation of the neutron fluence generated by the solar particle event of February 23, 1956, for a water and an aluminum-water shield-target configuration is then compared with LAHET and MCNPX Monte Carlo code calculations for the same shield-target configuration. The algorithm developed showed a great improvement in results over the unmodified HZETRN solution. In addition, a two-directional solution of the evaporation source showed even further improvement of the fluence near the front of the water target where diffusion from the front surface is important.				
14. SUBJECT TERMS Multigroup; Low-energy neutrons; Neutron transport; Evaporation neutrons; HZETRN; Radiation shielding			15. NUMBER OF PAGES 35	
			16. PRICE CODE A03	
17. SECURITY CLASSIFICATION OF REPORT Unclassified	18. SECURITY CLASSIFICATION OF THIS PAGE Unclassified	19. SECURITY CLASSIFICATION OF ABSTRACT Unclassified	20. LIMITATION OF ABSTRACT UL	